



## The E864 lead-scintillating fiber hadronic calorimeter

T.A. Armstrong<sup>a</sup>, K. Barish<sup>b,1</sup>, S.J. Bennett<sup>c</sup>, T.M. Cormier<sup>c</sup>, R. Cernejc<sup>c</sup>, A. Chikanian<sup>d</sup>, S.D. Coe<sup>d</sup>, R. Davies<sup>e</sup>, P.R. Dee<sup>c</sup>, G.E. Diebold<sup>d</sup>, P. Fachini<sup>c</sup>, E. Finch<sup>b</sup>, N.K. George<sup>d</sup>, S.V. Greene<sup>a</sup>, P. Haridas<sup>f</sup>, J.C. Hill<sup>g</sup>, A. Hirsch<sup>e</sup>, H.Z. Huang<sup>e,1</sup>, R.A. Hoversten<sup>g</sup>, B. Kim<sup>c</sup>, B.S. Kumar<sup>d</sup>, J.G. Lajoie<sup>b</sup>, Q. Li<sup>c</sup>, Y. Li<sup>c</sup>, B. Libby<sup>g,2</sup>, C.F. Maguire<sup>a</sup>, R.D. Majka<sup>b</sup>, M.G. Munhoz<sup>c</sup>, J.T. Murgatroyd<sup>c</sup>, J.L. Nagle<sup>d</sup>, A.N. Petridis<sup>g</sup>, I.A. Pless<sup>f</sup>, J.K. Pope<sup>d</sup>, C.A. Pruneau<sup>c,\*</sup>, J. Riso<sup>c</sup>, M.S.Z. Rabin<sup>h</sup>, J.D. Reid<sup>a</sup>, F.S. Rotondo<sup>b</sup>, A.J. Slaughter<sup>b</sup>, J. Sandweiss<sup>b</sup>, R. Scharenberg<sup>e</sup>, J. Sheen<sup>c</sup>, M. Tincknell<sup>e</sup>, A. Rimai<sup>e</sup>, G. Van Buren<sup>f</sup>, W.K. Wilson<sup>c</sup>, F.K. Wohn<sup>g</sup>, K. Zhao<sup>c</sup>

<sup>a</sup>Department of Physics, Vanderbilt University, Nashville, TN 37235, USA

<sup>b</sup>Yale University, HEP, New Haven, CT 06520-8122, USA

<sup>c</sup>Department of Physics and Astronomy, Wayne State University, Detroit, MI 48201, USA

<sup>d</sup>Yale University, WNSL, New Haven, CT 06520-8121, USA

<sup>e</sup>Department of Physics, Purdue University, West Lafayette, IN 47907-1396, USA

<sup>f</sup>Department of Physics, Massachusetts Institute of Technology, Cambridge, MA 02139-4307, USA

<sup>g</sup>Department of Physics and Astronomy, Iowa State University, Ames, IA 50011, USA

<sup>h</sup>Department of Physics, University of Massachusetts, Amherst, MA 01003, USA

Received 14 April 1997; received in revised form 11 July 1997

---

### Abstract

A large hadronic lead scintillating fiber calorimeter has been built and integrated into the AGS experiment E864 [C. Pruneau et al., E864 Collaboration, Proc. 6th Internat. Conf. on Calorimetry in High Energy Physics, 1996, Frascati, Italy; F. Rotondo et al., E864 Collaboration, Proc. Quark Matter'96, Heidelberg, Germany, 20 May 1996] spectrometer to provide an independent measurement of the mass of particles produced in heavy ion collisions. The “spaghetti-type” calorimeter design and construction techniques are described in detail. Results from a prototype and the full implementation of the calorimeter are reported. The hadronic energy resolution of the calorimeter is found to be  $\delta E/E = 0.035(\pm 0.005) + 0.344(\pm 0.008)/\sqrt{E/\text{GeV}}$ , in very good agreement with a FLUKA calculation. The hadronic time resolution is measured to be better than 400 ps. The combined calorimeter energy and time signals provide for a mass determination with good resolution. The mass resolution scales as  $\delta m/m = 0.026 + 0.347/\sqrt{E(\text{GeV})}$  for velocities  $v/c < 0.98$ . © 1998 Published by Elsevier Science B.V. All rights reserved.

PACS: 29.40 Vj; 25.75.-q

Keywords: Hadronic calorimeter; Strangelet search

---

\* Corresponding author. Tel.: +1 313 577 1813; fax: +1 313 577 3932; e-mail: pruneau@physics.wayne.edu.

<sup>1</sup> Present address: University of California at Los Angeles, Los Angeles, CA 90024, USA.

<sup>2</sup> Present address: Department of Radiation Oncology, Medical College of Virginia, Richmond, VA 23298, USA.

## 1. Introduction

A large scintillating fiber lead hadronic calorimeter has been built for AGS Experiment E864 [1,2] at the Brookhaven National Laboratory, a relativistic heavy ion experiment designed and built for a high sensitivity search of strange quark matter particles, called strangelets. The E864 search, conducted with a Au beam of 11.6A GeV/c impinging on Pb target, is designed to reach a sensitivity of approximately 1 part in  $10^9$  central Au + Pb collisions and should extend by many orders of magnitude the production limits reported by previous searches with both Si and Au beams [3,4].

Strangelets are predicted to be somewhat massive and expected to have a large mass-to-charge ratio [5]. If produced in relativistic heavy ion collisions, they are further expected to have a rapidity close to half the beam rapidity. The E864 apparatus, illustrated in Fig. 1, consists of a long flight path magnetic spectrometer [6] used to measure the particles' momenta and their times of flight in order to determine their mass with good resolution. It has been designed to operate at high rate and is fully capable of handling occupancies in excess of ten particles per event. The spectrometer comprises two magnets (labeled M1 and M2 in Fig. 1) that can be operated with magnetic fields as high as 1.5 T to sweep away the light particles (e.g. pions)

copiously produced in heavy ion collisions. A large vacuum vessel, located above the fiducial volume of the detectors and extending from the target area all the way down to the beam dump is used to enclose the beam and beam-like fragments exiting the target. This is done to eliminate possible interactions with air that would produce background. The detector systems include redundant tracking and time of flight detectors (S1,S2,S3,H1,H2,H3) and a large hadronic calorimeter. Further details about the spectrometer design, construction, analysis methods, and performance can be found in Refs. [6,7].

The calorimeter augments the spectrometer's particle identification by providing an independent measure of the particle masses based on time of flight and energy. It is designed to match the spectrometer acceptance and provide as hermetic and seamless a coverage as possible in order to optimize the energy resolution, maximize the detection efficiency and minimize the possibility of particle identification ambiguity. It consists of 754 identical towers mounted in a  $58 \times 13$  rectangular geometry. The individual towers are built with a longitudinally un-segmented "spaghetti" design. Lead and scintillating plastic fiber optics are used as the absorber and sampling material respectively.

Although the spaghetti design is conceptually fairly simple, its construction poses numerous

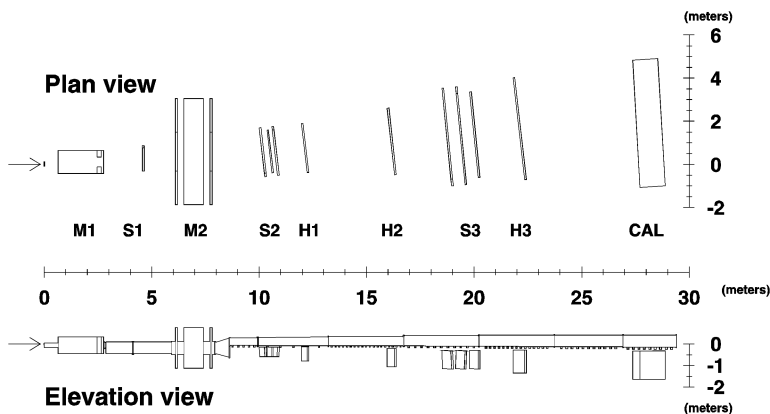


Fig. 1. Plan and elevation views of the E864 Apparatus. The beam direction and target position are indicated by the arrows. M1 and M2 are dipole magnets operated with B-fields up to 1.5 T, Straw tube chambers, S1, S2, and S3, provide accurate charged particle tracking. H1, H2, and H3 are large TOF hodoscopes. CAL is the hadronic calorimeter reported in this paper. The large vacuum vessel, only shown in the elevation view, is used to minimize interactions of the beam and heavy fragments downstream of the target.

technical challenges and a number of construction techniques have been reported in the literature [8]. The technique adopted for the construction of the E864 calorimeter is based on a lamination process by which scintillating fibers are sandwiched between lead plates with semi-circular grooves. The design and construction technique are described in detail in Section 2, where specifics of the calorimeter implementation within experiment E864 are also addressed.

In order to establish a “theoretical” reference by which one can predict and evaluate the calorimeter performance, simulations have been carried with the GEANT simulation package [9] and the hadronic shower program Fluka [10]. Of particular interest are the calorimeter energy resolution and its dependence with energy, the energy response, and the lateral shower profile. The simulation techniques and results are presented in Section 3. Other aspects of the calorimeter response such as the energy response to anti-protons are discussed in a separate paper [11].

The calorimeter implementation has proceeded in three stages. A  $4 \times 3$  prototype array was first built and tested with the AGS test beam during the summer of 1993. Results from a partial analysis of these data have been published elsewhere [12]. These and new results extracted from those data are presented in Section 4. A partial implementation of the detector, consisting of 180 towers, was completed for the 1994 AGS heavy ion run. The full detector configuration including  $^{60}\text{Co}$  radioactive source and laser calibration systems was completed and used during the fall 1995 heavy ion AGS run. Results obtained from the 1994 and 1995 runs concerning the calorimeter performance are presented in Section 5. The discussion focuses on the calorimeter energy response linearity, the energy resolution, the time of flight resolution, and the mass resolution. A summary of results characterizing the performance and conclusions is presented in Section 6.

The E864 experiment also features an innovative triggering system based on the calorimeter energy and TOF measurements used to enhance the experimental sensitivity to rarely produced particles such as anti-protons, anti-deuterons, or theoretically predicted exotica such as strangelets.

Strangelets are expected to be massive and produced at mid-rapidities. The triggering scheme consists of using the calorimeter to identify slow moving objects with a large energy, and is called Late Energy Trigger (LET). Its design and performance are discussed in a separate publication [13].

## 2. Calorimeter design and construction

The experimental design called for a large, seamless, and hermetic calorimeter coverage, matching the spectrometer fiducial acceptance, to measure times of flight and energies of hadrons with a good resolution, and provide an independent mass measurement. For practical purposes, a time resolution of 500 ps and an energy resolution of  $40\%/\sqrt{E}$  were set as targets [14]. Also, as the calorimeter is used in a large particle multiplicity environment and at very high rate, the chosen technology had to be fast and allow good detector granularity at reasonable cost. All these requirements can be readily met with a “spaghetti” sampling calorimeter design similar to that developed by the SPACAL collaboration [8] for experiments at the SSC and LHC colliders. The “spaghetti” design consists in using scintillating optical fibers embedded longitudinally in a high “Z” material.

Within the E864 apparatus, the calorimeter is located 27 m downstream of the target, and consists of 754 identical towers arranged in a  $58 \times 13$  rectangular array as illustrated in Fig. 2. The angular coverage in the horizontal (bending) plane is from  $-2.1^\circ$  to  $9.9^\circ$  and from  $-0.8^\circ$  to  $-3.3^\circ$  in the vertical plane.

The design of the calorimeter towers is described in Section 2.1. The construction procedure is detailed in Section 2.2. Specifics of the readout electronics are presented in Section 2.3. The  $^{60}\text{Co}$  and laser calibration systems developed for monitoring and calibrating the response of all towers are presented in Section 2.4.

### 2.1. Design

The E864 calorimeter tower design is illustrated in Fig. 3. The towers are built with a lead substrate.

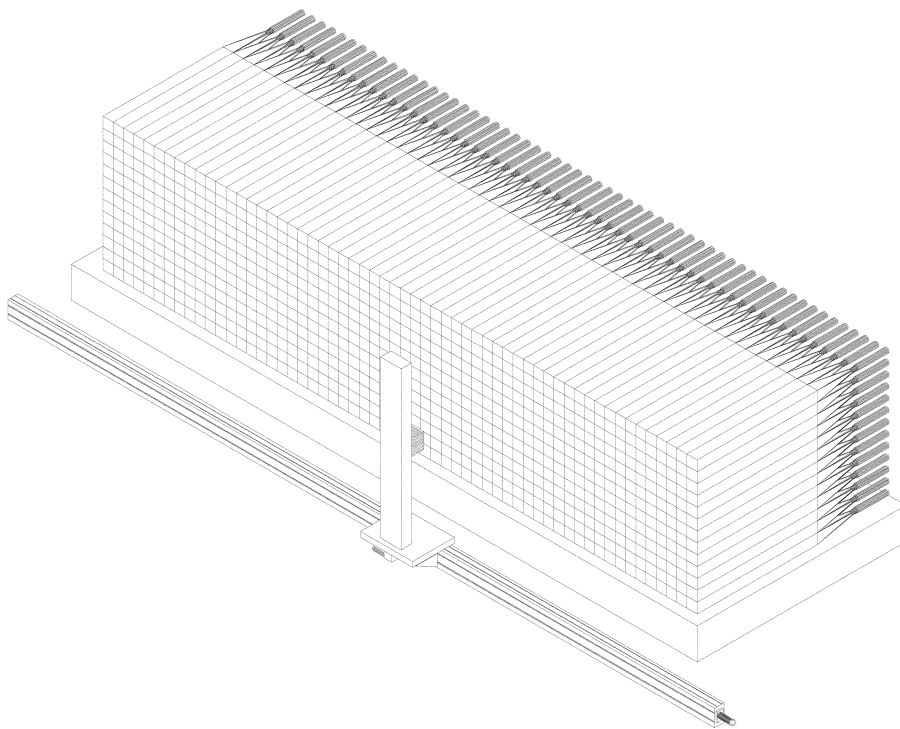


Fig. 2. View of the E864 Calorimeter and  $^{60}\text{Co}$  source transport calibration system. The calorimeter comprises  $58 \times 13$  towers mounted in a close packed geometry with no gaps between them. The tower design is based on a “spaghetti” design discussed in the text. Each tower is read out with a single PMT at the back.

Each tower has a  $10 \times 10 \text{ cm}^2$  cross-section and is 117 cm long. The back end of the tower is glued to a tapered light guide itself connected to a single photo-multiplier tube as illustrated in Fig. 3.

A cross-sectional view of a tower is presented in Fig. 4.  $47 \times 47$  scintillating fibers of 1 mm diameter are embedded within the lead substrate at regular intervals of 0.213 cm. These are used to sample the particle energy deposition and read out the scintillation light.

By design, the towers do not require any additional packaging and only a thin layer of epoxy paint is used to provide optical isolation. The outer layer of fibers lies 0.1 cm within the tower’s outer edges. The sides are uniform and flat so towers can be close packed. Close tower packing enables a consistent and regular fiber-to-fiber spacing, even across tower boundaries. The shower sampling is thus completely uniform across the entire calorimeter because there are no cracks or seams. Such

a design contrasts significantly with more traditional sampling calorimeter designs where wave-shifter plates or fibers are used to read out the scintillation light leading to dead or insensitive regions and position-dependent calorimeter response. This is especially important for a high-sensitivity experiment such as E864 where a non-uniform response due to cracks could possibly fake exotic events. The spaghetti design also provides for a good light yield and preserves the time response of the shower and scintillation processes, therefore allowing sub-nanosecond time-of-flight performance. These two aspects of the calorimeter performance are examined in Section 5.

Lead (Pb) was chosen as the absorber after theoretical calculations by Wigman [15] confirmed by experimental studies by Bernadi et al. [16] and independently by the SPACAL collaboration [8] had shown that calorimeter compensation as well as good hadronic energy resolution can be achieved

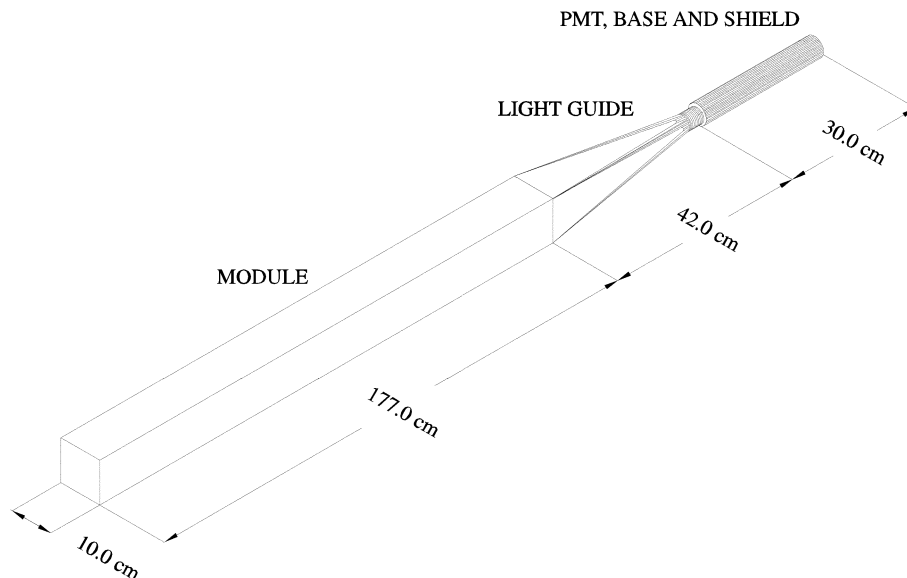


Fig. 3. Calorimeter Tower Layout. Scintillating fibers are imbedded longitudinally in a lead substrate. The light readout proceeds through a tapered lucite light guide with a single photo-multiplier tube per tower.

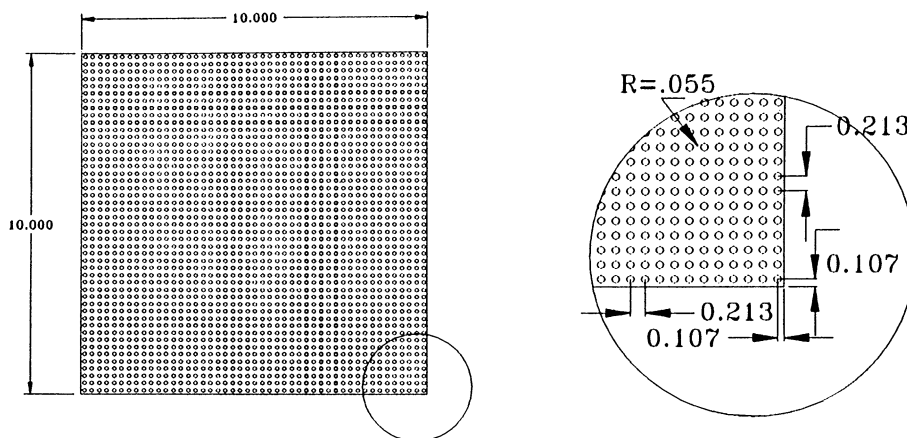


Fig. 4. Cross sectional view of a calorimeter tower:  $47 \times 47$  scintillating fibers are embedded in a square lead matrix with a regular 0.213 cm spacing. The insert shows the position and dimension of the fibers. All dimensions in cm.

with lead and scintillator instead of an expensive and difficult to handle uranium-based calorimeter. Lead, in contrast to uranium, has a lower neutron production cross-section that permits a faster response. A 1% admixture of antimony is added to harden the lead to a desirable mechanical strength and should have a negligible impact on the calorimeter performance.

Bicron BCF-12 [17] scintillating optical fibers are used as the sampling material. They were selected for their good light yield (50% of the yield obtained with anthracene), good transmission ( $1/e$  length  $\sim 2.2$  m), and fast response (decay time  $\sim 3.2$  ns). They are laminated between the lead plates and glued with Bicron BC-600 epoxy [17].

The tower front faces were covered with a light absorbing (black) epoxy paint to avoid light reflections from the front face. Although this somewhat reduces the total light yield of the towers relative to the maximum one could achieve by coating the front fiber end with a reflective material, it eliminates the problem associated with non-uniform reflectivity which could cause substantial tower-to-tower response fluctuations. A tapered light guide is glued using an optically coupling adhesive (Bicron BC-600) to the tower back face as illustrated in Fig. 3.

The light guide shape and dimensions were optimized by ray tracing calculations to enable uniform photon collection and transmission to the PMT photo-cathode from all  $47 \times 47$  fibers within a tower. Ultra-violet absorbing lucite was employed for the fabrication of the light guides in order to reduce the possibility that Čerenkov light created within the light guide might reach the PMT and deteriorate the energy response. The Čerenkov light might be generated by fast shower particles or albedo particles produced at the back of the calorimeter. The BCF-12 scintillator emission peaks at much longer wavelengths, 420 nm, than the Čerenkov radiation. The scintillation light suffers very little attenuation in the lucite and thus, only a small fraction of the true signal is absorbed while signal contamination is avoided.

The addition of a green filter to eliminate short wavelength has been considered but not included. Shorter wavelengths typically have shorter attenuation length in optical fibers. Shower development fluctuations combined with short attenuation lengths contribute to a constant term in the energy resolution. Eliminating the short wavelengths on the onset would therefore reduce this problem. However, a green filter would also block longer wavelengths to some degree and thus reduce the overall light yield. The stochastic contribution to the energy resolution would be worsened. Given that E864 is meant to measure particles of relatively modest energy, the stochastic term dominates the energy resolution and ought to be minimized. Green filters are not an interesting option for E864's calorimeter.

The towers have a lead to fiber ratio of 4.55:1 by volume similar to that used by SPACAL. It is expected to provide for good calorimetric compen-

sation and energy resolution. The average tower density is  $9.6 \text{ g/cm}^3$ . The effective radiation length ( $X_0$ ) is 7.8 mm. The nuclear interaction length ( $\lambda_I$ ) and the Moliere radius ( $R_M$ ) are 19.7 and 2.2 mm respectively.

## 2.2. Construction technique

Several “spaghetti calorimeter” construction techniques have been documented in the literature [8]. Studies have shown that the energy response depends critically on the uniformity of the fiber lattice. An irregular fiber lattice leads to sampling non-uniformities translating into a response which depends on the particle entry point and degrades the energy resolution. A practical construction technique was thus sought to ensure a good lattice uniformity with no irregular gaps between the fibers and the lead. The construction technique adopted is based on the lamination of lead plates and scintillating fibers.

The towers consist of a stack of lead sheets with rolled semi-circular grooves sandwiching the scintillating fibers. Special attention was given to the manufacturing process of the rolled sheets in order to minimize gaps and non-uniformities in the lead to scintillator ratio as well as optimizing the fiber lattice uniformity. In particular, stringent tolerances of 0.01 mm were applied on the shape and size of the grooves, and on the groove to groove distance. The 1% antimonial-lead sheets were grooved with a large rolling machine constructed at Wayne State University. An alternative construction technique based on the extrusion of lead plates with the semi-circular groove pattern, was considered too expensive. The rolling machine consisted of a free-rotating circular die with the negative profile of the desired grooves rigidly supported above a moving flat bed die 122 cm long which also had the negative profile of the grooves. Flat extruded lead (Pb) plates with a 1% antimonial admixture were placed on the lower die and rolled by pushing the lower die under the circular die. The lower die was driven by the saddle of a precision slide with a hydraulic force of 10 000 lb. It was found that the 1% antimony admixture produced roll-able plates while preserving enough mechanical strength and rigidity for stacking.

Residual bows and burrs that would prevent accurate stacking of the plates were removed prior to degreasing and cleaning the plates in a 10 ft tall trichloro-ethane vapor degreaser built specifically for that purpose. The lead plates thus cleaned were carried to a lamination facility for stacking and gluing. The lamination typically took an hour per module and involved the following stages; First, a lead sheet was placed on a flat metal base plate sprayed with mold release agent and BC-600 epoxy was liberally applied. Next, a pre-assembled ribbon of 47 fibers, approximately 120 cm in length, was smoothed into the semi-circular grooves manually. A new plate was then gently lowered and “keyed” into place on top of the raised ridges formed by the fibers. This process was repeated 46 times to complete a tower. The top and bottom sheets were half the thickness with grooves on only one side to allow for close tower packing with no gaps. At that point, the towers thus assembled typically contained a large excess of epoxy and were consequently too tall. Top and side steel 1 in thick plates shaped as a mold were added to the base plate on which the tower was laminated and were gradually clamped to form a rigid mold constraining the tower to the right cross-sectional size and straightening any residual bowing while squeezing the epoxy out of the mold. This process ensured the dimensional uniformity of all towers. Thus constrained, the towers were rotated by 90° to the vertical and BC-600 epoxy was poured into the top of the mold thus potting the fibers protruding from the lead matrix within a block of epoxy. Machining the critical back face (i.e. which transmits light to the light guide and PMT) of the tower was thus eased greatly and smearing of lead over the fibers ends was prevented. The towers were then cured in a large oven at a temperature of 105°F for a period of 24 h. The epoxy and fibers were machined and leveled with a fly cutter to enable a good light coupling with the light guide. The other end of the towers was also machined to even their surface and ensure that all towers were exactly the same length. Every tower was inspected visually for light transmission by shining a light at one end of the tower and verifying good transmission along all 47 × 47 fibers. Typically less than 0.2% of the fibers were found to be damaged in the lamination process and

had partial or no transmission. Finally, the front and side faces of the towers were painted with a thick, damage resistant, black epoxy paint to provide light tightness.

After careful cleaning, a light guide was attached (glued) to the 10 cm × 10 cm back end of the towers using BC-600 epoxy.

Finally, the light guides were wrapped with strips of non-wetting aluminized mylar film before being made light tight using several layers of PVC tape.

The handling of the completed towers was somewhat complicated by their 100 kg mass and the softness of the 1% antimony-lead alloy. Special packaging boxes were used for shipments of the towers and a number of special tools were designed to ease their stacking. The final positioning of the towers was done by hand.

### 2.3. Instrumentation and readout electronics

Philips XP 2262B [18] photo-multiplier tubes (PMT) were selected for the tower readout. A detailed study showed they have a good time response and good linearity over a wide dynamical range in spite of their relatively modest cost.

Each PMT was spring loaded into an individual housing assembly attached to bulkhead plates mounted on a large framework structure rigidly attached to the floor and the top of the calorimeter. The housing assemblies, illustrated in Fig. 5, were custom made of cheap commercially available plumbing components. The spring loaded assembly provided electrical and optical isolation as well as the 150 N force required to achieve good optical contact with a 49 mm diameter, 2 mm thick, Bicon BC-743A optical pad [17] between the PMT and the light guide. The bulkhead support plates were designed to also allow integration of a laser calibration system by providing room for the coupling of optical fibers to the light guides. The laser calibration system is described in more detail in the next section. The entire calorimeter forward of the bulkhead plates was covered in a common light tight enclosure whereas the bulkhead plates and the spring loaded base assemblies were wrapped individually.

Rather than using a conventional resistive bleeder chain base with costly external high-voltage

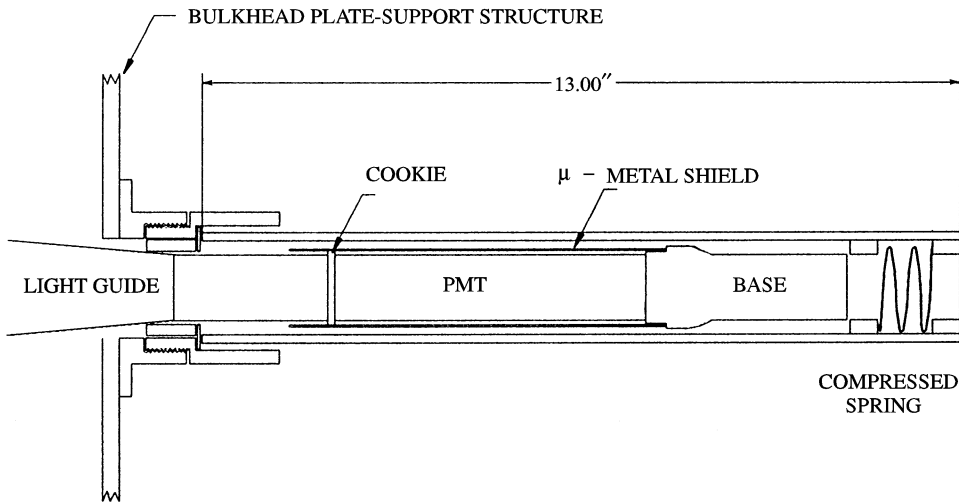


Fig. 5. PMT Mounting Assembly: A PVC wafer (cookie) is used to provide optical contact between the light guide and the PMT entrance window. A spring is used to maintain the cookie under compression and achieve good optical contact.

power supplies, N407 Cockcroft-Walton (CW) voltage generator bases designed and built by Nanometrics [19] were used to supply the PMT high voltages. These bases are also equipped with a leading edge discriminator used for the generation of time-of-flight (TOF) signals. Usage of “on-tube” discriminators allows a significant reduction in noise and signal deterioration and optimizes the calorimeter time response.

The linearity of the Philips XP2262B PMT/Nanometrics base combination was studied in detail using a nitrogen pumped dye laser system. The amplitude of the laser pulse was adjusted by a variable neutral density filter and measured by two unity gain vacuum photodiodes. The light output of the laser was calibrated in terms of energy based upon measurements made during the 1993 test beam. The linearity of each PMT/base pair was measured over a range of laser pulse amplitudes simulating energies varying from 300 MeV upto 50 GeV. With the high voltage of the base set so as to generate 400 pC, the maximum full scale range of the ADCs, for an input pulse equivalent to 50 GeV, the tube/base linearity was typically better than 1% over this range.

The CW bases are controlled by a series of DC levels carried along a ribbon cable together with

the necessary DC power. Such a system involves power distribution at low voltage and thus allows a considerable cost reduction relative to conventional resistive base systems. The DC control voltages are generated by a Nanometrics N-331/332 high-voltage control CPU system itself remotely controlled via an RS485 link by a personal computer. The N-331/332 control unit allows adjustment of individual voltages and discriminator settings in groups of fifteen. The actual high voltages are read back via a potentiometer in each base and digitized by an ADC, thus allowing continuous monitoring of the HV settings of all PMTs.

The analog and discriminated signals from the 754 towers were transmitted to the experiment counting house by means of 75  $\Omega$  miniature cables providing a delay of 380 ns required to form the trigger decision. The analog and digital signals reaching the counting house were split in order to feed signals to both the main data acquisition system and the Late-Energy trigger (LET). The analog signals are split on custom 9U Eurocard boards that house resistive splitting networks for each channel. These boards also provide a relay network to route any single channel to a lock-in amplifier of the  $^{60}\text{Co}$  calibration system instead of the main



DAQ/LET electronics. The digital timing signals from the PMT bases are regenerated on custom boards, designed and manufactured by LeCroy [20], to ensure timing stability before being split and converted to differential ECL for TDC input.

The analog pulse height signals and time signals were digitized with FASTBUS Lecroy 1881M charge integrating ADCs and Lecroy 1872A TDCs respectively. Both modules offer high resolution, fast data conversion and data sparcification. Only the time signals were zero suppressed however. All tower energy signals were read out in order to permit a detailed analysis of the energy shower shapes and avoid problems caused by slow pedestal drifts.

Flash ADCs and time-to-amplitude converters, with a coarser resolution, were used in the LET for very fast digitization of the signals in order to provide a second-level trigger. Further details about the design and operation of the LET can be found in Ref. [13].

#### 2.4. $^{60}\text{Co}$ calibration system

The purpose of the  $^{60}\text{Co}$  calibration system is to establish an initial relative gain adjustment for the 754 calorimeter towers and subsequently provide a tool to monitor and correct gain variations over an extended period of time. The absolute energy calibration of the towers, performed using tracked and well identified particles, is discussed in Section 5.2.

The calibration method consists of measuring the shifts in the output DC current of the PMT bases while exposing the towers (at their front face) to a strong (6 mCi)  $^{60}\text{Co}$  gamma ray source. Instead of using a charge integrating ADC with a long integration period for the determination of the baseline shift, an alternative method based on a single lock-in amplifier has been developed. The  $^{60}\text{Co}$  source is mounted in a lead pig with a rotating chopper assembly as illustrated in Fig. 6. The assembly is carried in front of the center of all towers in order to expose them to the modulated gamma ray flux produced by the source with the rotating chopper. A series of blades coupled with an opto-electronic switch is located beneath the assembly to provide a TTL reference signal in con-

stant phase relation with the radiation. This TTL signal is used to synchronize the lock-in amplifier integration.

Typical base currents produced by the source under normal operational conditions are around 10 nA. This current is fed via the relay system in the analog splitter boards into a low noise trans-impedance pre-amplifier and then to an EG&G 5105 lock-in amplifier [21]. The pre-amp is used to reduce the input impedance of the lock-in amplifier from 10 M $\Omega$  to an effective 10 k $\Omega$ . This is necessary to reduce the RC time constant of the delay cable/lock-in amplifier network to a level which is short relative to the 7 ms period of the chopper. Signals of typically 10 mV are measured with the lock-in amplifier using a 300 ms time constant while the towers are biased at their nominal (normal data taking) value.

A transport system, illustrated schematically in Fig. 2, has been built to carry the  $^{60}\text{Co}$  source assembly and position it successively in front of all 754 towers. The driving mechanisms for both horizontal and vertical axes of motion are lead screws driven by stepper motors remotely controlled by a PC running custom C++ software. A 400-line differential optical encoder is attached to the shaft of each motor to provide positioning information. In addition, accurate homing information on both axes is obtained by means of photomicrosensors. The combination of the optical encoders and photomicrosensors was found to be sufficient to obtain a positioning repeatability of approximately 0.5 mm over the entire front face of the calorimeter which measures  $5.9 \times 1.4 \text{ m}^2$ .

The radiation beam produced by the chopper assembly is collimated in order to permit full illumination of a single tower face so the response of all fibers can be sampled. The intensity measured in a given tower somewhat depends on the position of the source. Special care was thus taken to perform the calibration by positioning the source within 1 mm of the tower face center although mis-positioning the source by 5 mm results in less than 5% variance in the signal.

The  $^{60}\text{Co}$  system is used to determine and equalize the gains of all tower PMTs. Repeated measurements of given tower signals have a standard deviation of the order of 0.06 mV, i.e. roughly

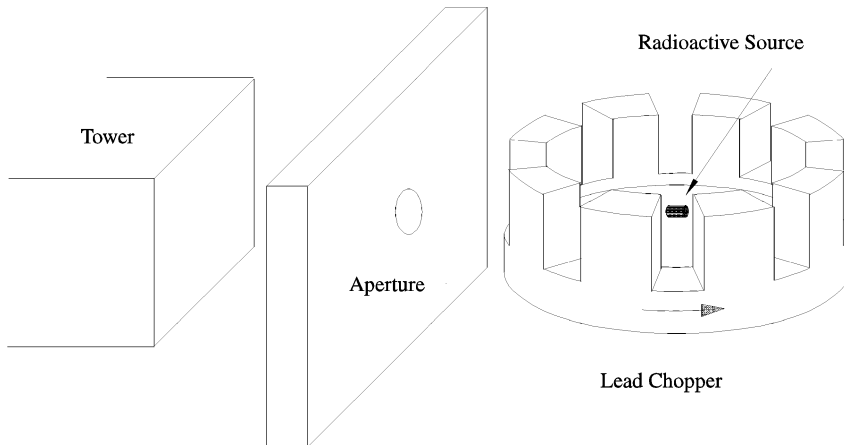


Fig. 6. <sup>60</sup>Co Rotating chopper assembly. A 6 mCi <sup>60</sup>Co is located at the center of the lead chopper rotating at a rate of 1000 rpm. The rotating chopper is surrounded with a 1.5 in thick lead shield. A single tower is irradiated through an half inch aperture in the shielding. The source/chopper assembly is moved sequentially in front of all towers to complete a calibration of the calorimeter.

0.6% of the signal amplitude. It is thus possible to set and equalize the tower gains with good accuracy. The gains of the towers forming the late energy trigger are equalized to within 5% providing an adequate trigger selectivity. Other tower gains are equalized to within 10%.

The tower gains are monitored with the <sup>60</sup>Co calibration system on a regular basis. The monitoring and calibration procedure is fully automated and controlled remotely from a personal computer. The PC controlled the source transport system and selects the appropriate PMT readout by the lock-in amplifier through a relay network on the analog splitter boards. The switching is controlled by a digital board (C7DIO48T [22]) integrated to the PC. Typically 10 successive measurements of the PMT DC voltage, interspersed with 300 ms delays, are made with the lock-in internal ADC. The mean and standard deviation of the 10 samples are calculated and logged. The automated successive calibration of all 754 towers requires roughly 2.5 h and is performed every 3 d or whenever the AGS beam is unavailable for extended periods of time.

### 2.5. Laser calibration system

Short-term variations of the gain of the calorimeter PMTs are monitored with a laser-based system flashing each PMT with a known amount of

light. The system, schematically illustrated in Fig. 7, is centered around a Laser Photonics LN300C nitrogen laser [23] producing 285 μJ pulses at a wavelength of 337 nm. The pulses are short, with a FWHM of 5 ns, and are produced at a repetition rate of up to 30 Hz. The 337 nm UV light is used to pump a dye laser operated with Stilbene-420 producing an output peaked at a wavelength of 420 nm chosen to match the emission profile of the BCF-12 scintillating fibers. The light beam produced by the laser is split in two parts by reflection from an uncoated quartz plate. The 4% direct reflection is incident upon the photo-cathode of a bi-planar PMT (ITT FW114A) whose output signal is used to generate ADC gates and TDC starts for the system with a time resolution of around 50 ps. The bulk of the light is transmitted through a remotely computer controlled variable attenuator into a 4.5 in diameter integrating sphere (IS) custom made by Labsphere [24]. The internal coating of the sphere consists of Spectralon [24]. It has a 99% reflectivity at 420 nm and thus considerably reduces light losses. The integrating sphere is used to mix and average the various spatial modes of the laser output which are known to fluctuate considerably over time. Two ports of the integrating spheres are used to monitor the laser intensity pulse by pulse with unit gain bi-planar photodiodes (Hamamatsu R1328U-02 and

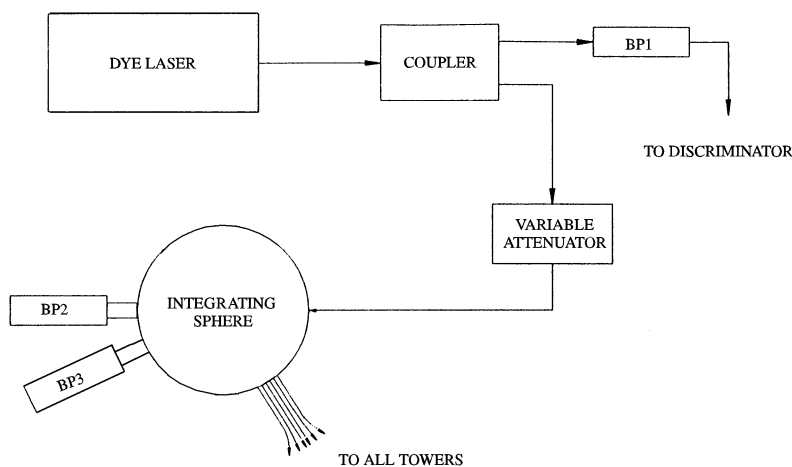


Fig. 7. Schematic of the laser calibration system. The light output from a dye laser is fed into a coupler/splitter. The first output of the coupler is connected to a biplanar (BP1) phototube to provide a trigger for the data acquisition system. The second output connects to a variable attenuator to control the light intensity fed into an integrating sphere. The integrating sphere is used to mix the various mode of the laser output. Two bi-planar phototubes are used to monitor the laser intensity on a pulse-by-pulse basis. The laser light is transmitted to all towers via fiber bundles made of 100  $\mu\text{m}$  diameter silica/silica fibers.

R1193U-02) [25]. Light is coupled to each of the 754 calorimeter PMTs by four fiber bundles, each containing 200 silica/silica fibers. The fibers are in 100  $\mu\text{m}$  diameter and feature a relatively small numerical aperture of 0.22. The bundles are connected to four independent ports on the IS through ferroelectric liquid crystal (FLC) shutters. The connection to each module is made by coupling the 100  $\mu\text{m}$  fibers to larger, 200  $\mu\text{m}$  diameter, hard silica fibers, glued into each tower light guide. The fiber-to-fiber connection is achieved using cheap but reliable VPIN splice bushings and connectors [26]. The large size and numerical aperture of the silica fibers ensure efficient light transmission to the PMTs.

The laser system was designed to shine light into at most one quarter of the input channels of each ADC at any one time, in order to limit the load in the input circuitry of the ADC. This is accomplished using LV050P-OEM FLC shutters from DisplayTech [27] customized for maximum extinction at 420 nm and operation at 35°C in custom mounts. These are bi-stable devices that can be switched from a dark opaque state to complete transmission by reversal of polarity of an externally applied 5 V signal. They have a relatively fast

switching time of 100  $\mu\text{s}$  and provide an extinction ratio of about 1000:1.

With the laser properly tuned and with “fresh” dye, less than 5% pulse-to-pulse amplitude variations can be obtained. However, the mean pulse height drops off quickly over a period of days as the dye ages. Moreover, in order to optimize the calorimeter energy resolution, a 1–2% pulse resolution was sought to minimize systematic effects. Two bi-planar phototubes mounted on the integrating sphere are used to monitor the laser intensity on a pulse-to-pulse basis. As they feature unity gain with great stability, they provide a stable short- to medium-term calibration reference. Temperature variations of the photo-cathode response of the photodiodes that could modify the output were minimized by keeping them at a constant temperature of 35°C with a temperature control system. The signals of all the calorimeter PMTs measured for laser pulses are corrected on a pulse-by-pulse basis to eliminate the effect of short-term fluctuations as well as medium term drift in the laser intensity. A typical laser spectrum measured with a typical calorimeter PMT during the run is shown in Fig. 8. The spectrum shown includes corrections for pulse-to-pulse variations of the

laser output determined with the two bi-planar PMT outputs. The peak relative width, of the order of 2%, is found to correspond to the photo-statistical limit. This point is discussed further in Section 5.8.

The laser was operated continuously during the 1995 and 1996/97 running periods. Typically a few “laser events” were interspersed and recorded during each beam spill. It was possible to track gain variation of the PMTs in detail over time. The system performance is discussed in Section 5.1.

### 3. GEANT simulation of the calorimeter response

Simulations of the energy response of the hadronic spaghetti calorimeter design discussed in this paper were performed prior to its construction in order to evaluate the adequacy of the design. Estimates of the energy resolution achievable with this design have been carried out with GEANT [9] using the GEISHA [28] and FLUKA [10] packages and have been reported in Ref. [29]. With calorimeter data now available, it is interesting to revisit the GEANT predictions and compare them with the measured performance of the detector. The simulations reported earlier concerning the energy resolution attainable with a finite array of towers have been repeated to take into account more accurate knowledge of the fiber attenuation length. The simulations were also used to evaluate the shower lateral profile, study the energy response high side tail and estimate the achievable position resolution.

#### 3.1. The simulation

The simulations were carried out using GEANT 3.21 and FLUKA. The calorimeter is simulated as

a seamless, crackless array of 121 towers mounted in a square  $11 \times 11$  geometry reflecting the actual geometry of the full detector implementation. The towers are  $10 \times 10 \text{ cm}^2$  by 1.17 m long modules. The calorimeter bulk material is lead (Pb) with a 1% antimony admixture. The plastic scintillating fibers were distributed within the lead in a regular  $47 \times 47$  regular lattice. The fibers were explicitly divided into two parts: a core of 0.8 mm diameter was used to simulate the active scintillation region and a radial shell 0.1 mm thick was added to simulate the fiber cladding and the glue used to bond the towers. Using the division technique available in GEANT, each tower was subdivided in horizontal strip themselves partitioned in unit cells containing one fiber, in order to minimize the computation time.

As in Ref. [29], the calorimeter signal is constructed from the energy losses of the shower particles in the active fiber medium, i.e. the fiber core. Saturation effects in the scintillator are included following Birks Law [30]. Finally, the finite attenuation length of the fibers, of the order of 2 m, was explicitly taken into account to evaluate the photon yield. All GEANT physical processes were activated. The shower particles were tracked to the lowest kinetic energy (10 keV) allowed in all media. Delta rays, explicitly generated, were tracked above the 10 keV cutoff.

Simulation were focused on protons in the kinetic energy range from 2 to 8 GeV most relevant for E864. In addition, some pion simulations have also been conducted for comparison with test beam data discussed in Section 4. Different calculations were carried out directing a simulated proton pencil beam at selected positions on the front face of the calorimeter array. The protons were injected in the calorimeter at an average angle of  $3.1^\circ$

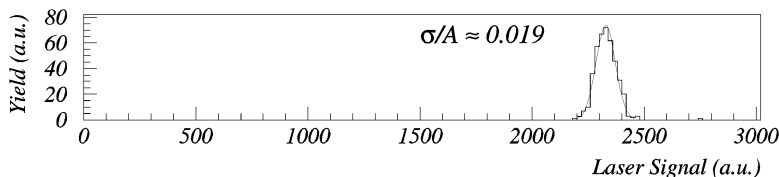


Fig. 8. Typical laser signal spectrum measured with a calorimeter tower PMT. The pulse height has been corrected for pulse-to-pulse variations of the laser output based on measurements done with the bi-planar phototubes. The corrected spectrum has a relative width (RMS) of  $0.019 \pm 0.002$ .

corresponding to the actual trajectories in the E864 spectrometer. Each calculation consisted typically of 5000 events, i.e. 5000 single protons shot into the calorimeter. A number of runs were also carried out using different incidence angles to examine the effect of the incidence angle on the response and resolution.

### 3.2. Simulation results

#### 3.2.1. Energy containment and resolution

Simulations of protons impinging at the center of an  $11 \times 11$  tower array were used to evaluate the shower containment and the energy resolution achievable with a finite size array of towers. A detailed lateral shower profile analysis is discussed in Section 3.2.2. Protons of 2, 4, 6, and 8 GeV kinetic energy were directed in the center of the array with a  $3.1^\circ$  angle of incidence. Negligible energy dependence of the profile was seen in the energy range considered. The results discussed below were obtained with 6 GeV protons.

The lateral shower containment is illustrated in Fig. 9 (top) which shows the ratio of the summed energy deposited in an array of  $n \times n$  towers to the total energy deposited in the  $11 \times 11$  array for  $n$  ranging from 1 to 11. The fraction of the total energy measured by the central tower amounts to only 50% and is lower for showers not initiated at the exact center of the array. A good containment ( $\sim 90\%$ ) is achieved with  $5 \times 5$  array. The convergence to full containment obtained with larger arrays is quite slow and makes full lateral containment somewhat impractical in a high-occupancy environment.

Fig. 9 (bottom) shows the predicted energy resolution as a function of the array size. Two methods are used to evaluate the resolution. In one (open circles), the resolution is estimated as  $\Delta E/E$  where  $\Delta E$  and  $E$  are the sigma and centroid of a Gaussian fit to the distributions. In the other (dark squares), the resolution is calculated as the ratio of the RMS of the distributions to their means. The small difference between the two methods arise from the slightly non-Gaussian shape of the energy response. The energy resolution achieved with a single tower is rather poor as a result of the relatively small fraction of the energy

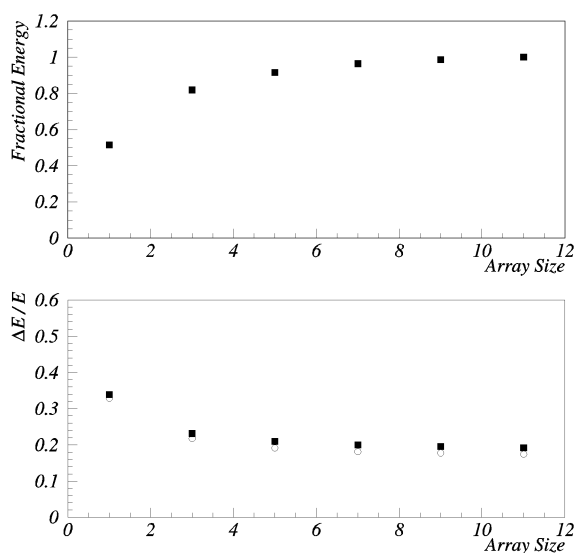


Fig. 9. GEANT FLUKA simulations of 6 GeV protons impinging at the center of an  $11 \times 11$  array. Top: fractional energy detected vs. summed array size,  $n \times n$ . Bottom: energy resolution vs. summed array size. Open circles are the ratio of Gaussian sigma to the Gaussian mean, Black squares are the ratio of distribution RMS and mean.

deposited in the central tower. A net improvement is obtained with  $3 \times 3$  and  $5 \times 5$  sums. It should be noted however that very little incremental improvement of the energy resolution is obtained by considering summed arrays larger than  $5 \times 5$ . Therefore,  $5 \times 5$  sums are used in the remainder of this analysis.

Fig. 10 shows the FLUKA prediction for the energy resolution calculated as the ratio of the RMS to the mean (black square) and the ratio of the Gaussian sigma to the mean (open circle) as a function of proton energy in the range 2–8 GeV. The difference between the RMS and Gaussian widths, of the order of a few percent, is a decreasing function of the energy, i.e. the predicted response tends to be more Gaussian at the higher energies. A fit to the Gaussian widths vs. energy yields  $\Delta E/E = (0.07 \pm .01) + (0.30 \pm 0.01)/\sqrt{E}$ , slightly at variance with Ref. [29] where the Gaussian widths had been extracted for  $11 \times 11$  sums and a longer attenuation length, 3 m, had been used. The effect of the finite attenuation length is to increase the ratio  $\Delta E/E$  by 1–2%. Given the finite

number of data points used in the fit, there is a strong correlation between the values of the constant and stochastic terms. Such correlation could partially explain the rather large constant term obtained in the fit. It is to be noted however that even without attenuation the resolution figures obtained from GEANT simulations cannot be satisfactorily fitted without the inclusion of a constant term. This may indicate that the chosen parameterization is inadequate.

### 3.2.2. Shower profile simulation

The lateral shower profile predicted by GEANT is characterized by calculating the average energy deposition in each of the  $11 \times 11$  towers for 5000 single protons impinging at different locations in the array. Calculations for a proton kinetic energy of 4 GeV are presented in this paragraph. Results obtained at other energies in the range 2–10 GeV do not differ significantly. The lateral shower energy deposition density is calculated as a function of the distance,  $r$ , to the center of the shower

$$\frac{dE}{dA} = \rho(r) \quad (\text{GeV/cm}^2) \quad (1)$$

which is parameterized, following Ref. [31], with the expression:

$$r\rho(r) = B_1 e^{-r/\lambda_1} + B_2 e^{-(r/\lambda_2)^2}. \quad (2)$$

Fig. 11 shows the average energy deposition (solid line) in the central row of the  $11 \times 11$  array for

protons impinging exactly at the center of the array. The dash line shows a fit to the distribution with the above parameterization. The parameter values are listed in Table 1 in Section 4.4.

Alternatively, Fig. 15 shows the average energy deposition in a tower as a function of the distance from the center of that tower to the particle hit position in the array. It is compared to profiles measured with a  $4 \times 3$  prototype array in Section 4.4. The 4 GeV proton simulation, shown as a dotted line, is compared to test beam data and the SPACAL parameterization [31]. The comparison to the test beam data is discussed further in Section 4 and [32].

### 3.2.3. High side tail

The calorimeter was primarily designed to make an independent measurement of a particle's mass, thus reducing particle identification ambiguities and enhancing the sensitivity of the search for strangelets. However, the common wisdom and available simulators at the time of the design could not guarantee that the spaghetti design would produce a Gaussian energy response at the comparatively low energies involved at the AGS. In particular there could be fluctuations leading to a large energy sampling mimicking the signal that would be left by a very massive particle.

Fig. 12 shows a simulated energy spectrum of 400 000 protons, with a kinetic energy of 4 GeV, entering the  $11 \times 11$  array in its center. The spectrum was obtained by summing only the central  $3 \times 4$  towers to enable a comparison with test beam experimental data. The predicted spectral shape is clearly non-Gaussian and a high side exponential tail is present. The exponential tail is however relatively steep, with a slope of approximately  $-1.5 \text{ 1/GeV}$  and extends down to many orders of magnitude. Note that a larger array coverage (viz  $5 \times 5$  and even  $11 \times 11$ ) only marginally increases the slope. Such a response, if achieved with the calorimeter, should not negatively impact the experiment sensitivity to high mass exotica. The high-side tail distribution shape was investigated explicitly with the prototype array tested at the AGS during the summer 1993 test beam. These experimental results are discussed in Section 4.

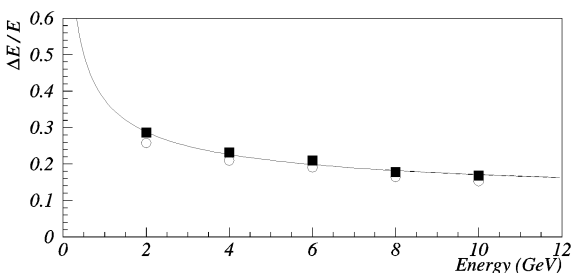


Fig. 10. Energy resolution vs. proton energy from GEANT FLUKA simulations. The estimates shown are based on  $5 \times 5$  tower energy sums. Symbols are defined as in Fig. 9, solid line is a fit to RMS points.

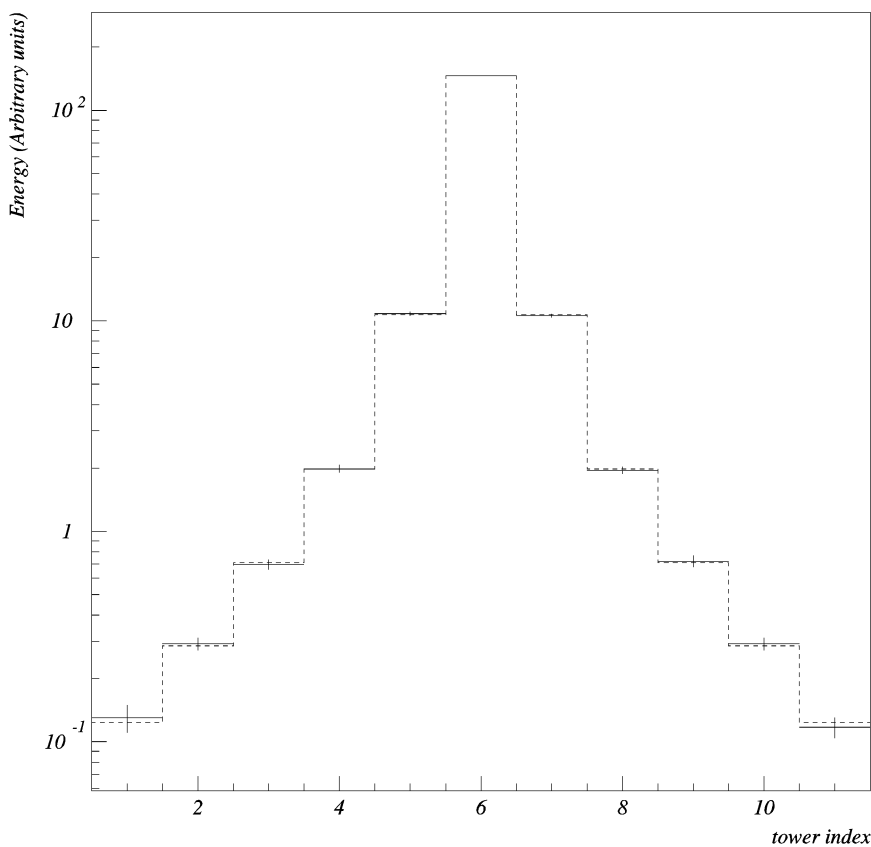


Fig. 11. GEANT/FLUKA simulation of the average energy deposited in the central row of an  $11 \times 11$  array for 4 GeV protons impinging in its center tower (tower index = 6). The solid line shows average energy depositions calculated from the GEANT simulation. The dash line shows a fit to the averages using Eqs. (1) and (2). Vertical error bars correspond to statistical errors only.

Table 1  
Lateral hadronic shower parameters: fit to data and GEANT simulations

Data Set	$B_1$ (GeV/cm)	$\lambda_1$ (cm)	$B_2$ (GeV/cm)	$\lambda_2$ (cm)	$\chi^2/\text{DoF}$
GEANT – 4 GeV	$0.020 \pm 0.003$	$16.3 \pm 1.1$	$0.0677 \pm 0.0008$	$4.90 \pm 0.07$	2.21
Test beam – 4 GeV	$0.030 \pm 0.015$	$10.5 \pm 4.0$	$0.078 \pm 0.010$	$3.12 \pm 0.43$	0.25
Test beam – 6 GeV	$0.055 \pm 0.021$	$8.1 \pm 2.0$	$0.087 \pm 0.010$	$3.26 \pm 0.43$	0.93
Test beam – 4 + 6 GeV	$(0.0082 \pm 0.0035)E$	$9.4 \pm 2.9$	$(0.018 \pm 0.003)T$	$3.09 \pm 0.45$	1.35
SPACAL [31]	$0.09 \pm 0.01$	$14.1 \pm 0.8$	$0.21 \pm 0.02$	$7.68 \pm 0.54$	

## 4. Prototype test

### 4.1. Goals of the in-beam study

A small  $4 \times 3$  tower prototype of the full calorimeter was built and tested during the summer of

1993 at the AGS test beam facility. The primary goals of the prototype were to identify possible problems in the design and components, to assess the time and energy resolution, to assess the response linearity, to study the energy deposition spectral shape and to compare the measured

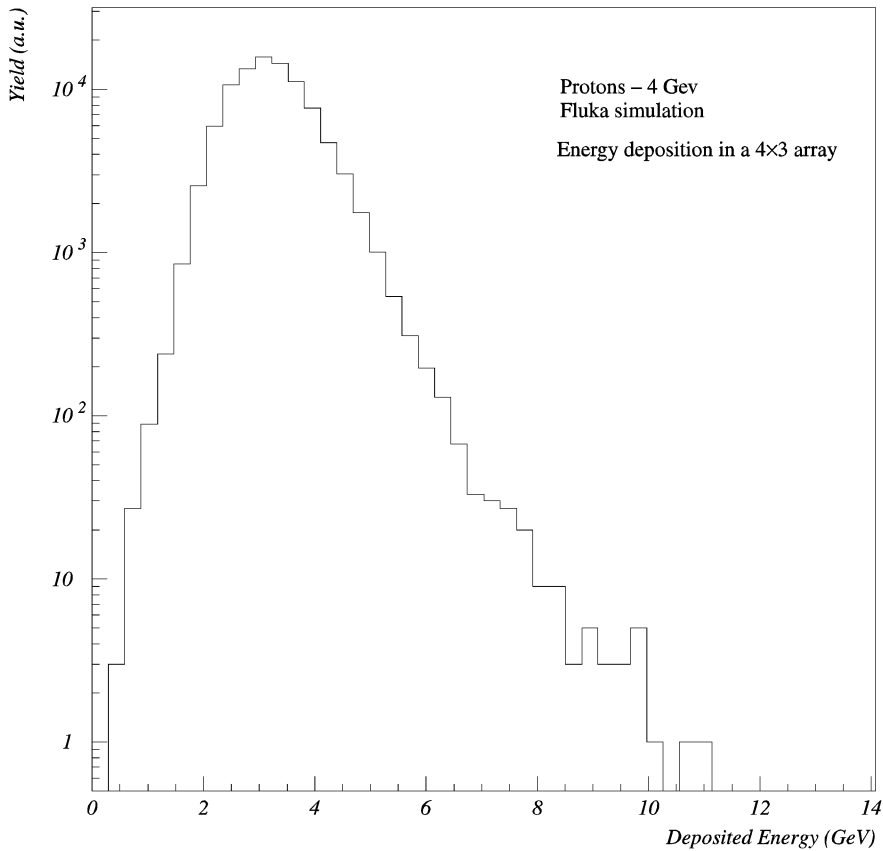


Fig. 12. Geant Fluka simulation of 4 GeV kinetic energy protons, incident upon the center of an  $11 \times 11$  tower array with angle of incidence of  $3.1^\circ$ . The energy is summed in a  $4 \times 3$  array surrounding the central tower for comparison with test beam data discussed in the next section.

performance with predictions from the Monte Carlo simulations. A subsidiary point of interest consisted in determining the hadronic lateral shower profile. Partial results concerning the energy and time of flight resolution measured with the prototype have been reported elsewhere [12]. It should be noted that thanks to improvements in the construction process and the quality control, the energy and time resolution performances obtained with the full detector implementation, discussed in the next section, were far superior to those achieved with the small prototypes. Thus, this section focuses on previously unreported results that are best obtained under test beam conditions. The experimental test setup and methods are described in Section 4.2. A study of the non-Gaussian high-

side tail energy response is presented in Section 4.3. Measurements of the lateral hadronic shower profile are reported in Section 4.4. Finally, Section 4.5 presents a study of the scintillation fiber optics transmission and attenuation length.

#### 4.2. Experimental method

The calorimeter prototype, precursor to the full implementation described in detail in Section 2 had basically the same design. The construction technique was however more primitive. Problems encountered during the construction of the prototype were eventually solved for the construction of the full detector. Of particular interest is the machining of the tower face coupling to the light guide. The



prototype coupling faces were leveled with a fly cutter machining off lead as well as the fibers. It was realized afterward that because the lead is more malleable than the fibers, the machining process tends to partially obscure the fiber ends with lead burrs thus substantially reducing the tower light yield. As described in Section 2, this was avoided in the full calorimeter construction by potting the fiber end with a thick layer of optical epoxy. Only the epoxy and fibers were machined and obstruction of the light was avoided.

The prototype was built with 2% antimonial-lead sheets with rolled semi-circular grooves 1.1 mm in diameter. The lead plates had been produced by a rolling process and had the desired malleability. However, lead plates purchased for the construction of the full calorimeter implementation were produced by extrusion. In the first shipment, plates were found to have considerably harder surfaces. For following shipments, the antimonial concentration was reduced to 1% in order to facilitate the rolling of semi-circular grooves.

The prototype detector consisted of 12 towers configured in  $4 \times 3$  rectangular array. The array was mounted on a bi-directional transport system to enable motion of the detector in a plane transverse to the beam axis. It was thus possible to vary the point of impact of the test beam into the detector. Furthermore, it was possible to tilt the detector longitudinally in order to study its response to particles entering at different angles of incidence.

The test beam consisted of a secondary beams of protons, pions, muons, electrons, and anti-protons produced by colliding the primary AGS proton beam on a thick target. The beam was directed into the detector by means of a narrow momentum acceptance (about 1%) beam line. Data were taken with fields of both polarities providing substantial samples of protons, electrons,  $\pi^\pm$ ,  $\mu$ , and even anti-protons.

A beam telescope, consisting of a number of scintillator counters, illustrated schematically in Fig. 13, was used to define a thin pencil beam, and to identify the particle species. The S4 counter, consisting of a thin scintillator, was used to trigger the data acquisition system and to define, in conjunction with the veto counters, the beam spot size

on the front face of the calorimeter. The counters S3 and S2, similar in size, were used to constrain the beam direction and measure, in conjunction with S4, the particle's time of flight providing the basis for particle identification. Large paddle detectors were positioned in front of the detectors and around the beam direction to veto the acquisition of events that could be triggered or contaminated by particles flying off the proper beam axis. The beam telescope also included two gas Cherenkov detectors, operated at atmospheric pressure, to tag electrons. Finally, a small counter was positioned behind the calorimeter to identify muons traversing the detector. The beam intensity was limited to a few hundred particles per second in order to limit pile-up and to operate the CAMAC based data acquisition system at a reasonable rate.

The calibration of all twelve modules/towers of the calorimeter was performed by sending 2 GeV/c electrons at the center of all towers. The detector array was tilted by  $3.1^\circ$ . The electromagnetic showers were nearly completely contained within the struck tower. Negligible energy deposition was measured subsequently in neighboring towers. The individual tower calibrations obtained were used to calculate the hadron's energy by summing the energy deposited in all 12 towers.

#### 4.3. High side tail energy response

The sensitivity of the E864 search for strangelets is in part determined by the calorimeter mass measurement. Specifically, as the calorimeter mass measurement is achieved on the basis of TOF and energy (calorimeter) measurements, it is imperative to fully understand both the TOF and energy responses of the calorimeter. Fluctuations of the hadronic shower energy deposition, in particular, could lead to an energy response with a very long high side tail that would limit the sensitivity of the experiment. Details of the energy response are difficult to predict accurately at the low energies involved in this work given the scant hadronic calorimetry data available at low energies. To remedy this situation, a significant body of proton and pion data was accumulated with the prototype calorimeter ( $\sim 2 \times 10^6$  events) in order to study the high side tail energy response.

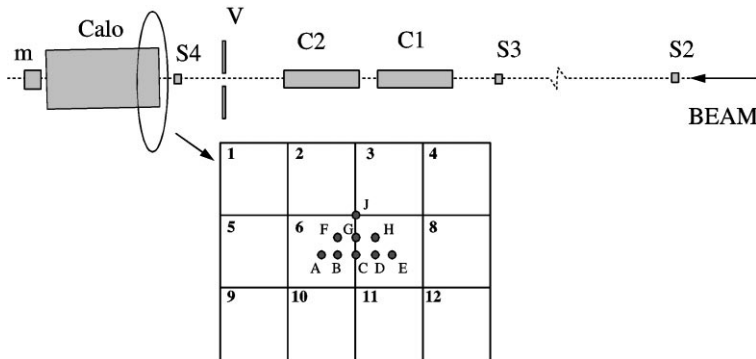


Fig. 13. Calorimeter prototype and test beam facility layout. S2, S3, and S4 are thin scintillator counters used to measure the particles' time of flight. C1 and C2 are threshold Cherenkov counters used to identify electrons. The "m" counter was used to identify muons traversing the calorimeter. The insert shows positions on the prototype front face where the beam has been directed.

Fig. 14 shows a  $\pi^+$  energy spectrum measured with beam line field settings selecting 4 GeV/c momentum particles. Tight purity identification cuts, based on the beam counters' time of flight and pulse height, and the Cherenkov counters were used to avoid contamination from protons and electrons, respectively, as they might distort the spectral shape. No correction for energy leakage beyond the  $4 \times 3$  array was applied. The mean detected energy is 3.23 GeV. This corresponds to 83% of the kinetic energy of the incoming pions. The missing energy,  $\sim 17\%$  leaks out beyond the  $4 \times 3$  array. This measured value is in good agreement with a Geant simulation presented in Section 3.2.1 where one also showed additional fluctuations of a few per cent are expected from the finite size array and should widen the measured distribution.

The spectral shape is clearly not Gaussian and features, as expected from the Geant/Fluka simulations (Section 3.2.3), a high side exponential tail. The tail is quite regular and extends down four orders of magnitude with a slope of  $-1.63 \pm 0.1$  1/GeV also in qualitative agreement with the GEANT/FLUKA prediction of  $-1.5$  1/GeV.

The calorimeter energy and time measurements are used by experiment E864 to evaluate the mass of the produced particles and to reject high mass candidates misidentified by the tracking system. Protons produced, for instance, by charge exchange reactions in the E864 vacuum vessel exit window, are expected to be the dominant source of back-

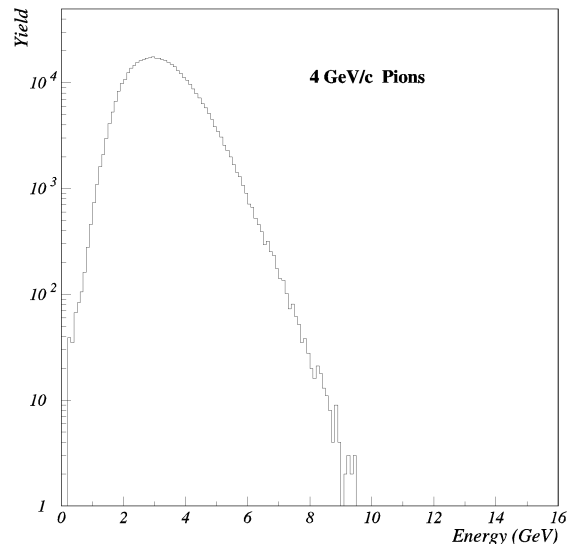


Fig. 14. Energy spectrum measured with a 4 GeV/c pion beam incident at position A, with an incidence angle of  $3.1^\circ$  into the test beam prototype array. The measured energy is calculated as the sum of the energy deposited in all  $4 \times 3$  towers. The mean energy detected is 3.2 GeV.

ground in the search for strangelets. Protons from this process would typically be reconstructed as charged heavy particles by the tracking system since they originate from locations beyond the analyzing magnet and look like high magnetic rigidity particles. An independent mass measurement performed with the calorimeter on the basis of the particle's energy and time of flight, with no

assumptions on the particle's origin, should reduce these backgrounds. However, the effectiveness of this additional constraint depends on the calorimeter energy resolution and spectral shape, i.e. the extent of the high side tail. The particle's mass is reconstructed with the expression  $m = E/(\gamma - 1)$  where  $E$  is the energy measured with the calorimeter,  $\gamma = 1/\sqrt{1 - \beta^2}$ , and  $\beta$  is determined on the basis of the TOF measurement performed with the calorimeter or the TOF hodoscopes. Considering 4 GeV protons impinging on the calorimeter, and using the spectrum of Fig. 14 at face value, one estimates the probability of measuring 3 times the proton mass using the above expression. According to Fig. 14, given the spectral mean of 3.2 GeV, the probability of measuring an energy larger than 9 GeV, or equivalently, overestimating the mass of a proton by more than a factor of 3, is of the order of  $10^{-4}$ . The calorimeter should thus in principle enable a rejection factor of 10000 or so in the search for heavy objects with a mass larger than  $3 \text{ GeV}/c^2$ . In practice, this rejection factor is somewhat reduced by overlapping hadronic showers in the calorimeter.

#### 4.4. Study of the lateral shower profile

Data from the  $4 \times 3$  prototype in test beam were used to determine the lateral (transverse) hadronic shower profile. Given the small size of the array, this was achieved by studying the energy deposition in particular towers (1,2,5,6) for different impact positions of the beam into the array. Impact positions used in this analysis are shown in Fig. 13.

Fig. 15 shows the measured energy deposition averaged over selected towers as a function of the tower-beam impact position distance. The data shown (cross) were obtained with 4 GeV/c protons. The horizontal bars correspond to the physical tower width of 10 cm. The vertical error bars include statistical and systematic uncertainties in the determination of the mean energy deposition.

Eq. (2), discussed in Section 3.2.2, was used to parameterize the lateral shower profile. The mean energy deposition in towers (1,2,3,6,7) for impact positions  $a-j$ , as defined in Fig. 13, was used to determine the shower parameters using a least square fit.

Based on data measured by the SPACAL collaboration, it was anticipated that the shower core should be small with  $\lambda_2 < 8 \text{ cm}$ . Given the finite tower size and the limited number of impact positions available for this analysis, fits involving only the exponential term were first performed to determine the shower decay length  $\lambda_1$ . The fits included only data for impact positions greater than 5 cm. The  $\lambda_1$  values thus obtained were used as a seed in a 4 parameter fit of all the data. The fit  $\chi^2$  and parameter values obtained with 2, 4, and 6 GeV/c protons are listed in Table 1. Also listed for comparison are parameters for a 6 GeV/c beam extrapolated from SPACAL data and parameters extracted from a fit to a Fluka simulation.

Fig. 15 shows the fitted function of Eq. (2) for 4 GeV/c protons. The overall agreement of the parameterization with the data is excellent. However, the  $\chi^2/\text{DoF} \sim 0.25$  is rather low and suggests the errors have been overestimated. As expected, the Gaussian core has a small size with  $\lambda_2 = 3.1 \pm 0.4$ . The exponential term has a decay length of  $10.5 \pm 4.0$ . The parameters of the fit and the  $\chi^2/\text{DoF}$  are listed in Table 1. The dashed line shows a profile calculation based on SPACAL parameters extrapolated to 4 GeV/c from their shower profile measurements in the 10–150 GeV/c momentum range [31]. The SPACAL profile, shown in Fig. 15, is in good agreement with the data of this work. Small differences in the tail might be attributed to difference in the construction of the SPACAL and E864 calorimeters. It is to be noted that the 10 MeV energy deposition difference observed between the SPACAL profile and this work's data at a distance of 20 cm corresponds to a 2 ADC channel difference and should not be overemphasized as it is within the uncertainty of this measurement. For further comparison, Fig. 15 also shows a fit to the output of a GEANT/FLUKA calculation. The FLUKA fit is in better agreement with the SPACAL data than this work's data. This should come as no surprise given that FLUKA has been mostly tuned on the basis of high-energy measurements. The agreement with this work's data is however sufficient to warrant the use of FLUKA at the energies involved at the AGS provided the lateral shower size is not overly critical. FLUKA predicts a somewhat longer shower

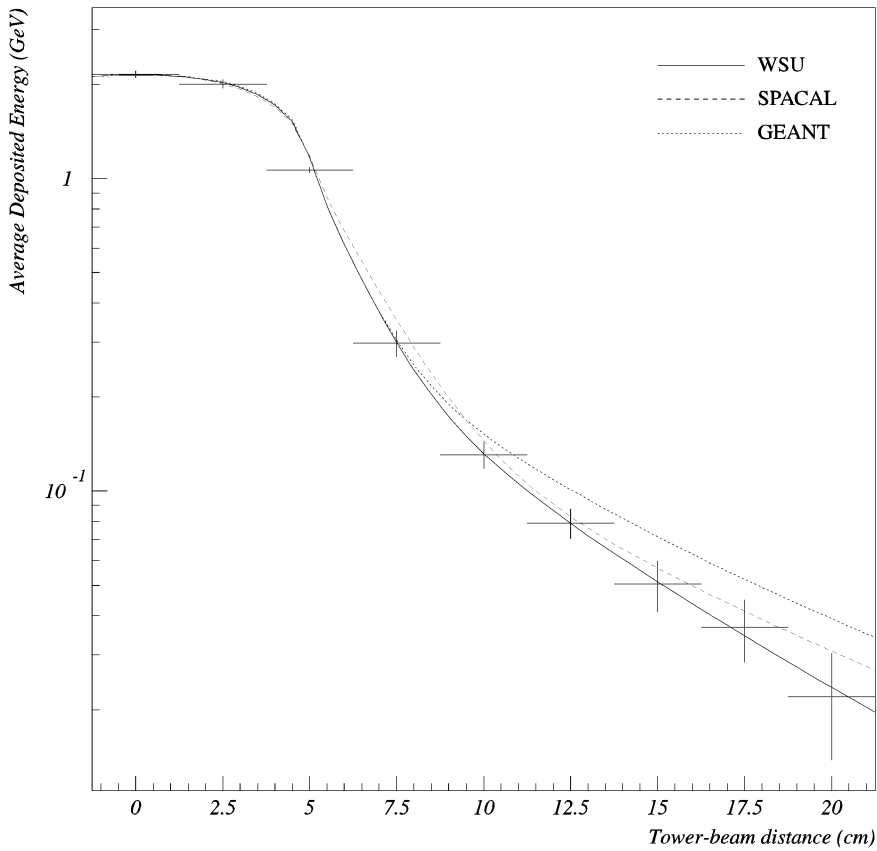


Fig. 15. Comparison of the lateral shower profile measured with the prototype (cross = data, solid line = fit to the data), with a fit to Geant simulation (dotted line), and the SPACAL lateral shower parameterization (dashed line).

tail than that measured. Taken at face value, the data shown imply FLUKA underestimates the shower containment in a  $5 \times 5$  tower array by 10% or so.

#### 4.5. Scintillating fiber attenuation length

The  $4 \times 3$  tower prototype was used to evaluate the light attenuation length of the scintillating optical fibers *in situ*, i.e. embedded in a lead matrix and surrounded by optical epoxy. To do so, use was made of the movable “ $x$ - $y$ ” table on which the prototype was mounted during the test beam run. Rather than directing the beam at the front face of the calorimeter towers, the prototype assembly was rotated by  $90^\circ$  in the horizontal plane so as to expose the side of the towers to the beam. Using the

“ $x$ - $y$ ” table, it was then possible to move the towers in the plane transverse to the beam direction and have the beam enter the towers in different locations along their length. 2 GeV electrons, selected with Cherenkov counters, were used for this study.

Fig. 16 shows a plot of the measured energy (open circles) as a function of the beam entrance position in tower #1. The beam entrance position is measured relative to the tower back face, i.e. the interface to the light pipe. The error bars are statistical only. The solid line shows a fit to the data with a two exponential function

$$E(x) = C_l \exp(-x/\lambda_l) + C_s \exp(-x/\lambda_s). \quad (3)$$

The dashed line shows the fitted long component only. The fitted coefficients, and  $\chi^2/\text{DoF}$ , are

listed in Table 2 for data measured with towers 1, 5, and 9. The long components as measured with the 3 towers are in agreement, within errors, with one another. They are also found to agree quite well with the BCF-10 fibers' nominal  $1/e \sim 190$  cm length published by BICRON [17].

## 5. Full calorimeter implementation performance analysis

All 754 towers of the calorimeter were assembled prior to the 1995 Au-beam run at the AGS. They were all fully functional and operational. The  $^{60}\text{Co}$  and laser calibration systems were also fully operational. The calorimeter was used to take data during the 11.6 GeV/c/u Au-beam to search for strangelet production and for the study of relativistic heavy ion collision dynamics. Many aspects of the calorimeter performance were studied and monitored during the entire heavy ion run. The calorimeter performance in terms of noise and gain stability is reported in Section 5.1. The energy calibration procedure is described in Section 5.2. It essentially relied on charged particle tracks reconstructed with the spectrometer. These were also used to study the energy response linearity, the energy, time, position and mass resolutions reported in Section 5.3, Section 5.4, Section 5.5, Section 5.6, and Section 5.7 respectively. Finally, calibration data obtained with the laser calibration system are interpreted in terms of calorimeter photon yield in Section 5.8.

### 5.1. Noise and gain stability

Particular attention was paid during the assembly of the calorimeter and associated electronics to

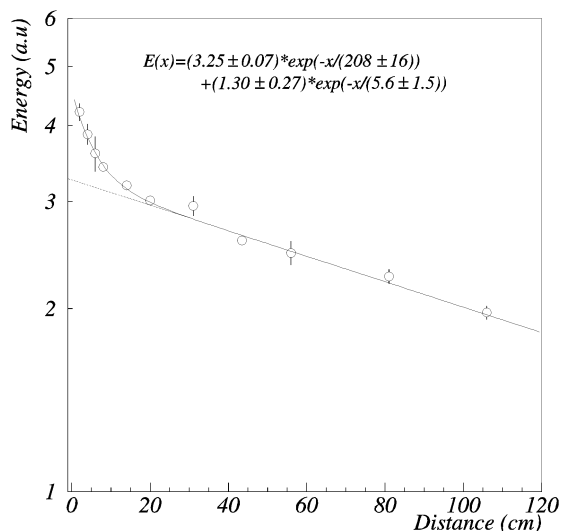


Fig. 16. Light attenuation length: energy measured (in arbitrary units) in tower 1 as function of the electron beam entrance position along a tower side. The error bars are statistical only. The solid line shows a two exponential fit to the data. The dash line displays the long component of the fit.

the elimination of ground loops and other sources of electrical noise. All electronic channels were consequently very quiet. The analog signals from all towers, for instance, had typically a pedestal RMS width of 3 ADC channels or less, corresponding to a noise of less than 150 fC after integration over a 80 ns gate. Given the gain of 6.3 MeV/ADC channel (see discussion in Section 5.2), this corresponds to an equivalent noise of less than 18 MeV per tower and is negligible compared to the calorimeter resolution. The correlated noise was estimated by comparing the pedestal width (RMS) of energy sums of groups of  $5 \times 5$  adjacent towers with the sum of the RMS of all 25 towers calculated

Table 2

Longitudinal light attenuation: coefficients and  $\chi^2/\text{DoF}$  of a two exponential fit to the energy measured as a function of the beam entrance position in towers 1, 5, and 9

Tower	$C_s$ (a.u.)	$\lambda_s$ (cm)	$C_l$ (a.u.)	$\lambda_l$ (cm)	$\chi^2/\text{DoF}$
1	$1.30 \pm 0.27$	$5.6 \pm 1.5$	$3.25 \pm 0.07$	$208 \pm 16$	1.1
5	$0.48 \pm 0.10$	$12.4 \pm 5.4$	$3.64 \pm 0.12$	$161 \pm 12$	2.4
9	$0.95 \pm 0.44$	$24 \pm 13$	$3.2 \pm 0.5$	$202 \pm 54$	0.5

individually. These were obtained during normal data taking with special “pedestal triggers” interspersed between “physics triggers”. The magnitude of the correlated noise was found to depend on the hit occupancy and data acquisition rate. At low occupancy and rate, the correlated noise amounted to approximately 20 ADC channels for a  $5 \times 5$  sum corresponding to a contribution of 5 MeV/tower to the energy resolution. At the highest rate and occupancy, the correlated noise term was found to increase up to 14 MeV/tower. The tower-to-tower signal correlations during the 1995 run were found to arise from minor voltage drops within the PMT base power supplies. They were easily corrected for during the 1996/97 run. The most dramatic effect of the voltage drop at high rate was to cause a 1–2% gain shift. It was possible to explicitly measure the gain shift rate dependence tower by tower using the Laser calibration system. Small gain corrections (0–2%) based on the instantaneous beam rate measured with the beam counters were applied on an event by event basis.

The pedestal values of all analog signals (energy) were monitored regularly during the run. Shifts of typically less than 3 ADC channels were observed over periods of many hours. These shifts, although small, were explicitly accounted for in the data analysis discussed below.

The gain stability of the PMTs was also monitored using both the  $^{60}\text{Co}$  and the laser calibration systems. Gain measurements were performed with the  $^{60}\text{Co}$  calibration system approximately every three days. The laser system was also operated continuously to monitor short-term gain variations. The gains of most PMTs were found to be rather stable. Typically, gain variations of less than 4% were measured over the entire 8 week run. For periods of a few hours, the gain variations were typically limited to 2% or less. These variations were monitored and corrected for with the laser system for all data analyzed and presented in this section.

The accuracy of the laser calibration system was evaluated by comparing the laser calibrations with  $^{60}\text{Co}$  calibrations made at the same time. It was found that for towers with significant gain variations ( $> 2\%$ ) the laser and  $^{60}\text{Co}$  calibration systems provided correction coefficients in good

agreement with each other. The correction factors obtained independently with the two systems were however found to be uncorrelated if the gain variations were less than 1–2%. The reliability and accuracy of the two calibration systems is thus estimated to be of the order 1–2% or so. Such a performance is completely satisfactory for the gain stability and energy resolutions needs of E864.

## 5.2. Energy calibration

The absolute energy calibration of the calorimeter was performed with well reconstructed and identified particle tracks produced by the 11.6A GeV/c Au beam impinging on a Pb target. The track reconstruction was done using an algorithm presented in detail in Refs. [6,7] and included all relevant data from the three TOF hodoscopes H1, H2, and H3 as well as the straw tube chambers S2 and S3. Data obtained with different field settings (0.45, 0.75 and 1.5 T) were used to provide samples of different particle species and maximize the energy range examined. The high rate achievable with the E864 data acquisition system enabled the detection of a large sample of light nuclei such as deuterons and tritons produced in central Au + Pb collisions, in addition to protons. A comparison of the calorimeter response to protons and light nuclei can provide insight into the response to strangelets.

The calorimeter tower gains were first equalized according to gain measurements performed with the  $^{60}\text{Co}$  calibration system. Minor gain corrections of the order of 1–2% determined with the Laser calibration system were also applied. The absolute energy calibration coefficients were determined by comparing the (un-calibrated but gain equalized) energy measured with the calorimeter with the kinetic energy of protons, deuterons, and tritons tracked into the calorimeter.

The kinetic energy of the particles,  $E$ , is evaluated from the reconstructed track momentum and the mass of the identified particles. To avoid ambiguities, a number of stringent tracking cuts were applied to insure good particle identification and sample purity. The cuts included the selection of particles with a velocity,  $\beta < 0.975$ , a fiducial cut (i.e. tracks are required to originate from the target

within 1 cm), and finally  $\chi^2$  cuts are applied on linear fits in the  $xz$ ,  $yz$ , and  $tz$  planes.

Fig. 17 shows a typical mass spectrum reconstructed by the tracking system with a 0.45 T field setting. The contamination in the deuteron and triton peaks is estimated to be smaller than 5% for  $\beta < 0.975$ . Similar or lower contamination levels are achieved with the other field settings.

The identified tracks were projected to the calorimeter front face to search for a matching energy cluster. The cluster position was determined by an algorithm discussed in the next section. A match is defined by requiring the distance between the track projection at the front face and the cluster position is smaller than 10 cm. In order to limit ambiguities and distortions, only tracks impinging within  $\pm 1.5$  cm of the center of the calorimeter towers are used for the determination of the tower gains.

Possible tower-to-tower differences in the light transmission attenuation length are neglected. Studies of the light attenuation reported in Section 4.5 showed the towers have attenuation lengths  $\sim 200$  cm with tower-to-tower differences of the order of 20 cm or less. As the construction techniques used in the full calorimeter assembly were improved and a stringent scintillating fiber quality was applied, we expect the full implementation to have even less attenuation length variations than the prototype detector. The fiber quality control included measurements of the fiber attenuation length as well as the fiber diameter. The impact of these variations on the overall calorimeter resolution is estimated to be 1–2% and is thus considered to be negligible.

The terms  $E_{3 \times 3}$ ,  $E_{5 \times 5}$ , and  $E_{7 \times 7}$  are defined to be the sum of the energies in  $3 \times 3$ ,  $5 \times 5$ , and  $7 \times 7$  tower arrays, respectively, surrounding a leading tower. The leading tower is taken as the tower, within a cluster, with the largest energy, whether it is actually pointed at by a track or lying next to such a tower.

Shower merging and shower contaminations are considerably reduced by selecting showers that satisfy the condition  $E_{7 \times 7} < 1.5E_{3 \times 3}$  and demanding that the  $5 \times 5$  towers forming a cluster measure the same time of flight within  $\pm 3$  ns. A tighter time cut only marginally improves the sample purity at the expense of statistics.

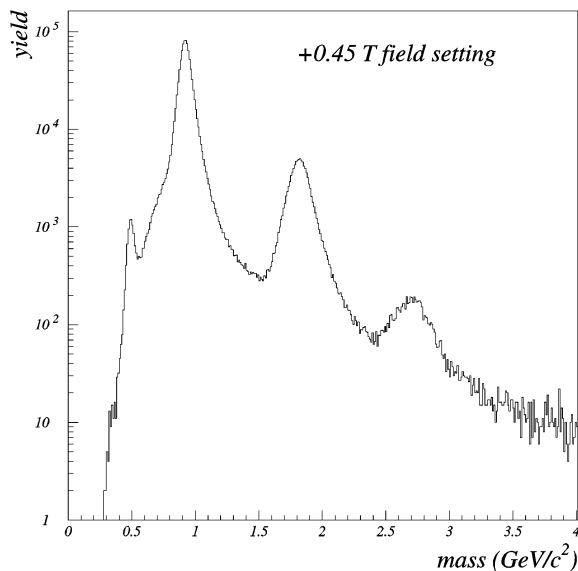


Fig. 17. Distribution of mass reconstructed with the H1, H2, H3, S2, S3 detectors for particles with  $\beta < 0.975$ . Proton, deuteron, and triton peaks are clearly seen at the correct masses. The sharp cutoff at mass  $\sim 0.5$  is due to the  $\beta$  cut. The kaon peak is accordingly truncated.

Fig. 18 illustrates the calibration procedure. The  $E_{5 \times 5}$  energy sums, in ADC channels, are plotted as a function of the track energy, in GeV, for well reconstructed tracks. The dark circles indicate the most probable  $E_{5 \times 5}$  energy in each track energy bin. A linear fit, constrained to pass through the origin, was used to determine the calorimeter energy gain.

The gain calibration was determined independently with samples of protons, deuterons, and tritons reconstructed under different field settings to examine the possibility of saturation effects (with higher mass or energy deposition) and gain variations with time. The fitted gains are listed in Table 3. Gains determined with different particle species are consistent to within 3%. The momentum resolution of the tracking spectrometer was estimated with a detailed Monte Carlo simulation including all relevant detector volumes and physical effects to be of the order of 2% or better for momenta below 8 GeV/c. This estimate is confirmed by the observed excellent mass resolution of 3% or better at  $\beta < 0.975$ . Systematic errors on the

momentum scale are evaluated from deviations of the reconstructed masses from the actual particle masses to be of the order of 2% also. The fitting procedure involved in the determination of the energy calibration was estimated to a systematic uncertainty of the order of 2% in addition to statistical uncertainties associated with finite data sample. Accounting for all these effects, the energy calibration systematic error is estimated to be less than 6%.

### 5.3. Energy response linearity

Fig. 19 shows a plot of the average relative energy difference  $(E_{5 \times 5} - E)/E$  as a function of the particle momentum. Protons (circle), deuterons (square), and tritons (triangle) were obtained with a 1.5 T data set. Only minor deviation from linearity ( $< 2\%$ ), are seen for protons. Slightly larger deviations ( $< 5\%$ ), are observed for deuterons and tritons.

### 5.4. Energy resolution

The energy resolution of the calorimeter is evaluated by comparing the  $E_{5 \times 5}$  energy sum to the reconstructed track energies used as a reference. Fig. 20 shows a typical plot of the relative energy difference  $(E_{5 \times 5} - E)/E$  for tritons of energies ranging from 9 to 10 GeV. As the relative energy difference spectra are nearly Gaussian, the width of a Gaussian fit to the data,  $\Delta E$ , is used in this work to characterize the energy resolution. Use of the RMS of the energy distributions produces resolution figures larger by 1–2% in agreement with the simulations discussed in Section 3.2.1.

Fig. 21 shows a plot of the relative width,  $\Delta E/E$ , as a function of the track kinetic energy for protons (circle), deuterons (square), and tritons (triangle). The tracking energy resolution, which amounts to 3–4%, has not been unfolded. The data shown is based on tracks with  $\beta < 0.985$ . Because the observed composite particles are produced at central rapidities, they have larger momenta than protons with the same  $\beta$  and thus populate different regions of the plot. One sees that, wherever there is overlap, similar resolutions are measured for the three particle species investigated. In view of the good energy

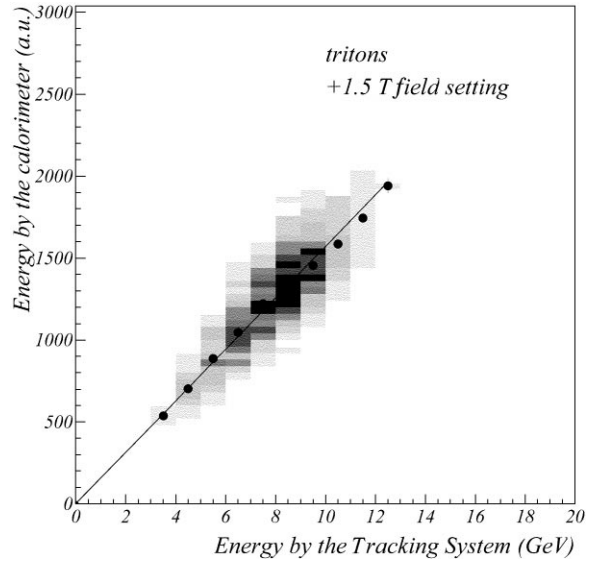


Fig. 18. Scatter plot of the cluster energy,  $E_{5 \times 5}$ , as a function of the kinetic energy of the track,  $E$  for tritons measured at + 1.5 magnetic field setting. The dots indicate peak positions taken for different bins of track energy,  $E$ . The straight line shows a fit to the data including the origin.

Table 3

Energy calibration coefficients evaluated with different particle species under different field settings. The errors listed are statistical only

Particle species	Field (T)	Gain (MeV/ADC channel)
Protons	0.45	$6.21 \pm 0.02$
Deuterons	0.45	$6.31 \pm 0.05$
Deuterons	1.5	$6.33 \pm 0.11$
Tritons	1.5	$6.43 \pm 0.02$

linearity noted earlier and the similarity of the energy resolution response for the three species, it appears that there are no saturation effects and one can expect a similar calorimetric behavior for other, heavier, particle species such as strangelets.

A fit to the relative width including all three particle species yields

$$\sigma(E)/E = (3.5 \pm 0.5)\% + \frac{(34.4 \pm 0.8)\%}{\sqrt{E \text{ (GeV)}}} \quad (4)$$

and is shown as a dashed line in Fig. 21. With a stochastic term of the order of 34%, the spaghetti



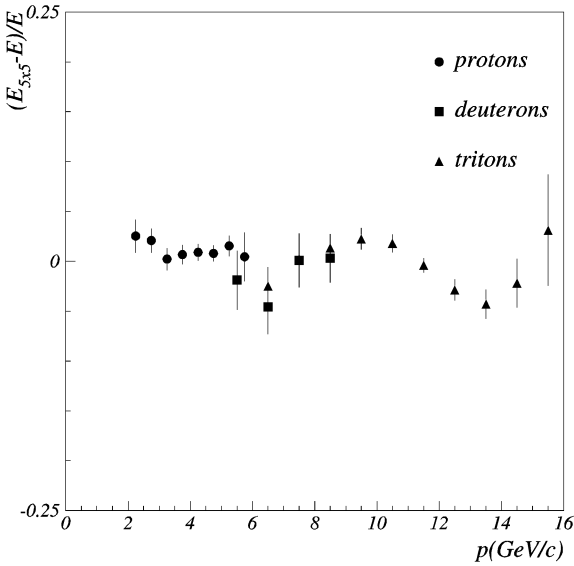


Fig. 19. Average relative energy difference  $(E_{5 \times 5} - E)/E$ , plotted as a function of the track momentum,  $E$  for reconstructed protons (circle), deuterons (square), and tritons (triangle).

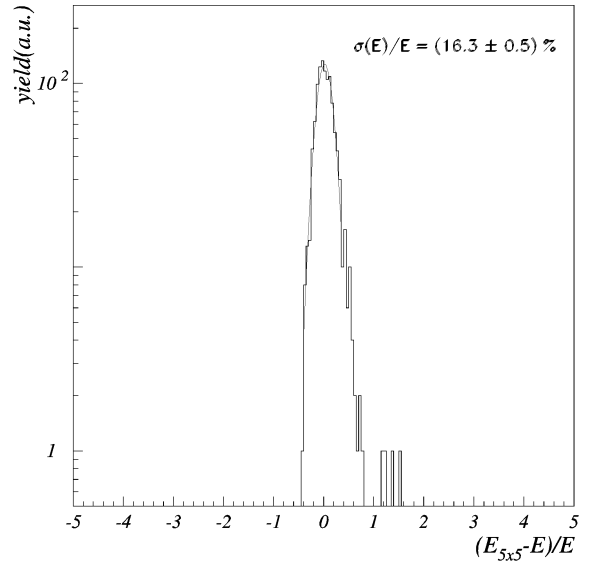


Fig. 20. Relative energy difference  $(E_{5 \times 5} - E)/E$  for tritons of energies ranging from 9 to 10 GeV.

calorimeter design clearly outperforms more conventional designs involving wavelength shifters. The resolution achieved also satisfies with a good safety margin the E864 experiment design requirements.

In Fig. 21, the stars show the resolution predicted with GEANT Fluka for protons as described in Section 3.2.1. The agreement between the data and the simulation is excellent. At the lowest energies measured, Fluka slightly underestimates the fluctuations possibly owing to an excessive neutron production. At the highest momentum considered, 10 GeV/c, the predicted resolution is slightly larger although not entirely inconsistent with the resolution measured with tritons.

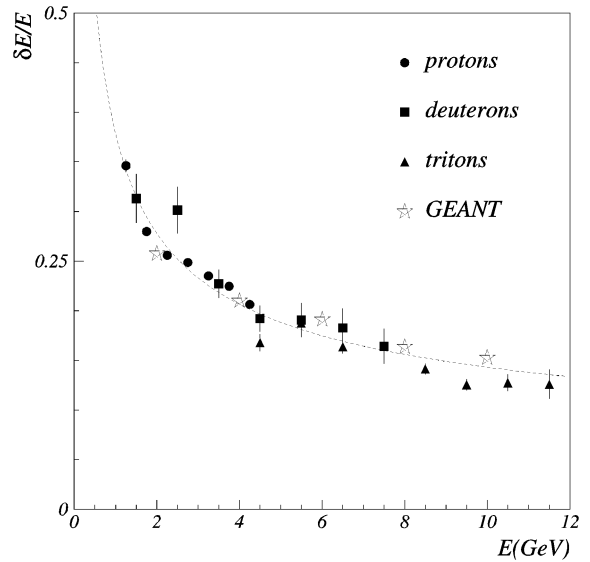


Fig. 21. Energy Resolution vs. particle's energy: protons (circle), deuterons (square), and tritons (triangle), Geant simulation for protons (stars). The dotted line shows a fit (Eq. (4)) fit to the data.

### 5.5. Time of flight resolution

The direct readout of the scintillation light with longitudinal scintillating fibers enables a relatively precise measurement of the particle's time of flight ased on leading edge discriminators included in every photomultiplier base.

The particle's time of flight,  $T_{\text{calo}}$ , is determined from the energy cluster leading tower (i.e. the tower

with the largest energy) using the following relation:

$$T_{\text{calo}} = T_0 + T_{\text{slew}} - T_{\text{offset}} \quad (5)$$

$T_{\text{offset}}$  corresponds to a simple TDC offset.  $T_0$ , or time zero, corresponds to a physical propagation

time from the target to the tower for speed of light particles.  $T_{\text{slew}}$  is the TDC signal corrected for slewing effects.

The offsets  $T_{\text{offset}}$  and time zeros  $T_0$  are determined individually for each tower. The  $T_0$  are constants which depend solely on the magnets field settings. The offsets  $T_{\text{offset}}$  are constants determined run by run to correct for minor variations of the delay cables, PMTs and TDCs operating conditions.

The signal  $T_{\text{slew}}$  is determined from the cluster leading tower TDC signal. Slewing effects produced with the “on-tube” leading edge discriminators are corrected using the following ansatz:

$$T_{\text{slew}} = T_{\text{lead}} + a + b/\sqrt{E} + \exp(c + dE) \quad (6)$$

$E$  is the energy measured by the leading tower. The coefficients  $a$ ,  $b$ ,  $c$ , and  $d$  were determined by a fit to the  $T_{\text{lead}}$  vs.  $E$  slewing curve measured with photons. Measurements of the PMT signals with waveform digitizers performed during the 1993 prototype in-beam test showed electromagnetic and hadronic showers have nearly identical signal shapes. Slewing effects should thus be independent of the particle type and are best determined with photons rather than hadrons as one avoids uncertainties associated with track reconstruction, track curvature, particle velocity, and time of flight determination. Photons were identified in the calorimeter as narrow clusters where more than 95% of the energy is deposited in the cluster central tower. By contrast, hadrons have typically a much wider lateral shower profile with the fraction of the total energy deposited in the central tower amounting to less than 95%.

Fig. 22 shows a plot of the calorimeter time,  $T_{\text{calo}}$ , vs. the track extrapolated time at the calorimeter front face based on the three TOF hodoscope measurements,  $T_{\text{hodo}}$ . The plot shows triton track data measured with a 1.5 T field setting. The measured calorimeter time is seen to scale quite linearly with the track projected time.

Fig. 23 shows a plot of the typical time difference  $T_{\text{calo}} - T_{\text{hodo}}$  for tritons with momenta ranging from 9 to 10 GeV/c. The distribution is Gaussian with a width of  $388 \pm 10$  ps. The low side tail is attributed to soft photon pile-ups in the cluster

leading tower. The time resolution has been studied for protons, deuterons, and tritons as a function of the particle’s momentum and is shown in Fig. 24. In the energy range considered, the time of flight resolution shows little dependence on the momentum. However, there is some indication that better resolution is obtained with tritons at the highest momenta measured.

The finite time resolution of the three TOF hodoscopes amounts to roughly 150 ps [7] per plane and is somewhat negligible relative to the time width shown in Fig. 24. One concludes that the calorimeter time-of-flight resolution is of the order of 400 ps or better. It comfortably exceeds the 500 ps TOF resolution design set forth for the E864 experiment [14].

### 5.6. Cluster position determination and position resolution

The finite shower size allows for a determination of the shower position based on the energy sharing between neighboring towers. Following previous works [33], various methods were examined to determine the shower position. Best results were obtained with the energy weighted average defined as follows:

$$x_{\text{ew}} = x_0 + (10 \text{ cm}) a_{\text{ew}} \frac{\sum_{j=i-1}^{i+1} (j-i) E_j}{\sum_{j=i-1}^{i+1} E_j} \quad (7)$$

where  $x_0$  refers to the center position of the tower,  $i$ , with the maximum energy.  $E_j$  refers to the energy measured with tower  $j$ . The towers are 10 cm wide.  $a_{\text{ew}}$  is a coefficient that needs to be determined. A similar expression is used to determine the cluster vertical position.

Fig. 25 shows a plot of the position  $x_{\text{ew}}$  as a function of the extrapolated track position on the front face of the calorimeter. The constant  $a_{\text{ew}}$  was adjusted to 2.7 so the slope of the correlation is unity. The triangles show the mean evaluated in different slices of  $x_r$ . The solid line shows a fit to the data.

Fig. 26 shows the RMS,  $\delta_x$ , obtained from a Gaussian fit to the position difference in different bins of  $x_r$ . The RMS of the distributions averages to

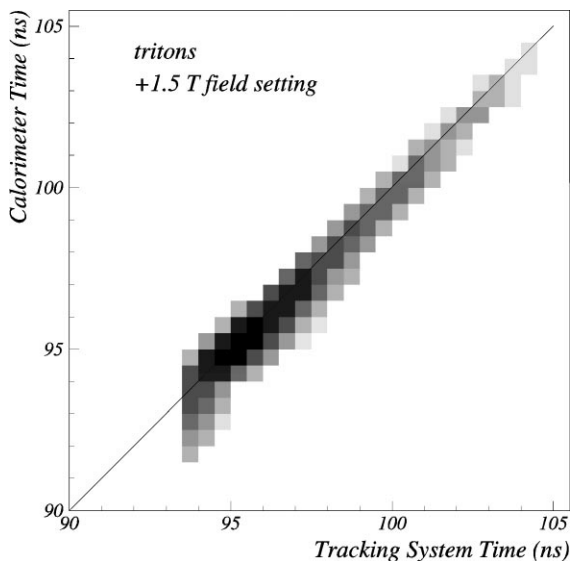


Fig. 22. Triton time of flight measured with the calorimeter vs. hodoscope extrapolated time at the calorimeter front face.

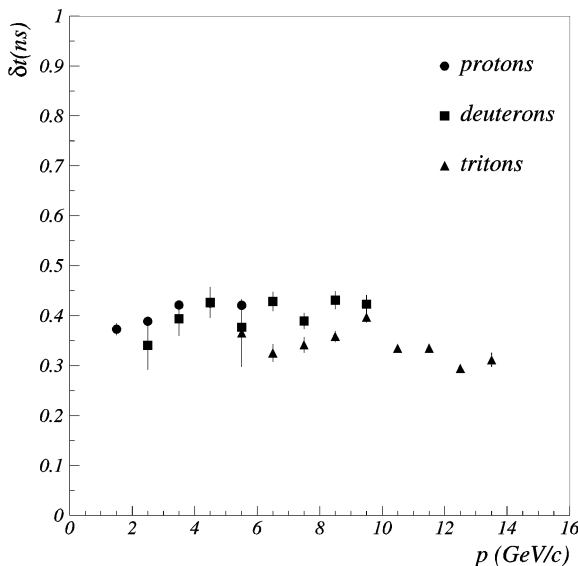


Fig. 24. Calorimeter time-of-flight resolution as a function of the particle momenta: Protons (circle), Deuterons (square), Tritons (triangle). Errors are statistical only.

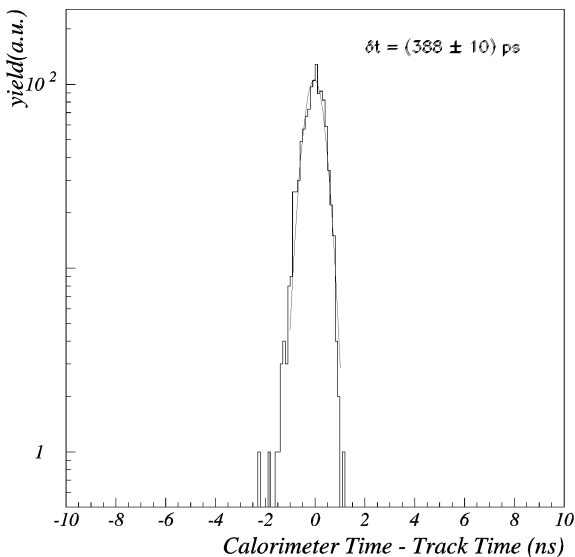


Fig. 23. Time difference  $T_{\text{calo}} - T_{\text{hodo}}$  for  $9 < p < 10 \text{ GeV}/c$  tritons measured under a 1.5 T field.

values below 2.8 cm for positions well within a tower but is somewhat larger for hit positions near the edge of a tower. The accuracy of the track projection on the calorimeter front face is of the

order of 1 cm. The position resolution achieved with the energy weighted mean is approximately 2.5 cm. This value is slightly better than the average error,  $10/\sqrt{12} = 2.88 \text{ cm}$  incurred if the hit position is simply assumed to be at the center of the struck tower. This modest performance arises from large fluctuations of the finite and small energy deposition in neighboring towers. It is, however, sufficient to enable unambiguous calorimeter hits and track matching.

### 5.7. Mass reconstruction

The calorimeter was added to the E864 apparatus to provide a redundant measurement of the particles' masses in order to eliminate particle identification ambiguities that may arise in track reconstruction and thence augment the experiment's sensitivity to rare particles. Also, the capacity to determine the particle's mass independently, i.e. without the tracking system, enables the study of neutral particles such as neutrons, high energy photons, and possibly anti-neutrons.

The reconstruction of the mass,  $m$ , relies on both the measurement of the deposited energy,  $E$ ,

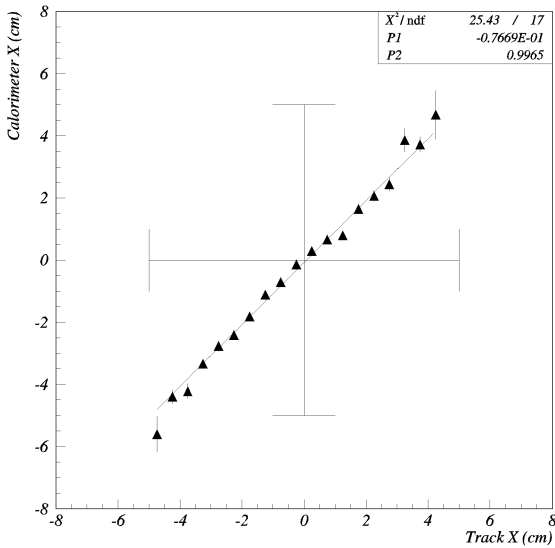


Fig. 25. Cluster position (calorimeter X) as a function of the extrapolated track position (track X). The cluster position was determined with the energy weighted method of Eq. (7). The cross illustrates the dimensions of a tower. The error bars are statistical only. The solid line shows a linear fit to the data. The fitted parameters are shown in insert.

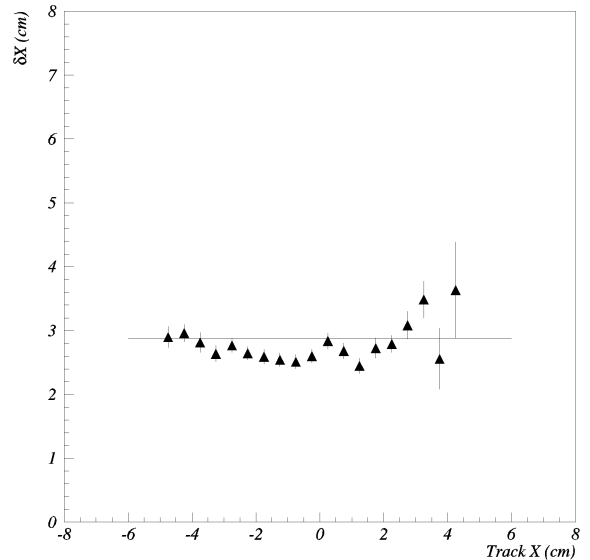


Fig. 26. Position resolution as a function of the position of incidence on the front face of a tower based upon the extrapolated track position (track X). The position resolution,  $\delta x$ , is calculated as the RMS of the difference  $x_{\text{ew}} - x_{\text{track}}$  where  $x_{\text{ew}}$  is calculated with Eq. (7) and  $x_{\text{track}}$  is the track extrapolated position (track X) on the front face of the calorimeter.

and the time of flight performed with the calorimeter.

$$m = E/(\gamma \pm 1) \quad (8)$$

where  $\gamma = 1/\sqrt{1 - \beta^2}$ , and  $\beta$ , the particle's velocity, is calculated using the particle's trajectory length and the measured TOF. The  $-$  and  $+$  are used for baryons and anti-baryons respectively.

Fig. 27 shows reconstructed mass spectra obtained for well identified protons (top), deuterons (middle), and tritons (bottom) in the momentum range  $2 \text{ GeV}/c < E < 3 \text{ GeV}/c$ ,  $8 \text{ GeV}/c < E < 10 \text{ GeV}/c$  and  $10 \text{ GeV}/c < E < 11 \text{ GeV}/c$  respectively. Tracking and cluster cuts similar to those used for the energy calibration have been used to ensure sample purity and avoid shower contamination. The spectra shown illustrate the nearly Gaussian mass response observed at all energies.

Fig. 28 shows a plot of the average mass reconstructed as a function of the particles momentum. Protons, deuterons, and tritons identified with the tracking systems are shown. The extent of the energy range presented for all three particles is

determined by the  $\beta < 0.985$  cut used in the track reconstruction. The plot illustrates that over the selected energy range which also corresponds to the useful energy range, the calorimeter mass response is almost independent of the particle's momentum. The high side tail seen in the reconstructed deuteron mass spectrum is mainly due to cluster contamination by merging clusters.

Fig. 29 shows the mass resolution,  $\delta m/m$ , calculated from the Gaussian width (sigma) of the mass spectra, as a function of the particle's energies. The mass resolution of protons, deuterons, and tritons are shown with dark circles, squares, and triangles, respectively. The data shown were obtained at the 0.45 and 1.5 T field settings. The particle species have been identified by combined TOF and momentum information from the tracking system. The data shown is limited to energy and velocity ranges where particle identification is unambiguous and contamination is limited to less than a few per cent.

The solid line, in Fig. 29, corresponds to the function  $\delta m/m = 0.026 + 0.347/\sqrt{E(\text{GeV})}$ , which

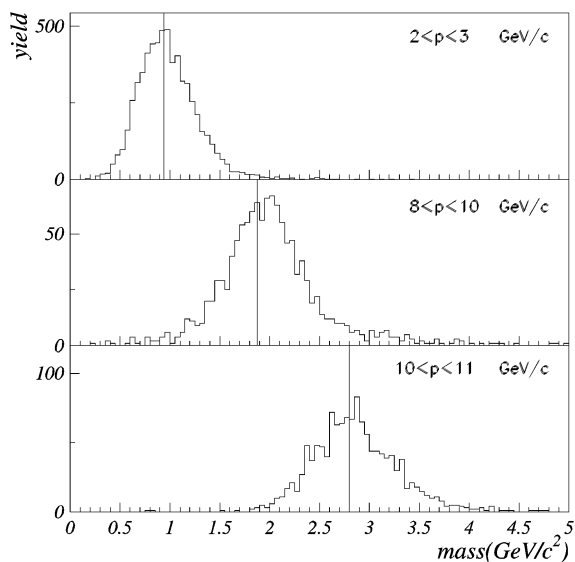


Fig. 27. Calorimeter reconstructed mass protons, deuterons, and tritons for momentum intervals  $2 \text{ GeV}/c < p < 3 \text{ GeV}/c$ ,  $8 \text{ GeV}/c < p < 10 \text{ GeV}/c$ ,  $10 \text{ GeV}/c < p < 11 \text{ GeV}/c$ , respectively. Solid vertical lines show the particle masses.

has the same functional form as the calorimeter energy dependence. It illustrates that the mass resolution is mainly dominated by the energy resolution. For  $\beta > 0.975$  (e.g.  $E > 3.5 \text{ GeV}$  protons) however, a departure from this simple relationship is observed, for all three species, as a result of the finite time resolution.

Based on the above expression for the mass resolution, one estimates the mass resolution for heavier particles and (light) nuclei. This is of special interest for the E864 search for charged and neutral strangelets. The calorimeter mass measurement is used to confirm the charged particles mass measurement made with the tracking and time of flight detectors. It also provides the only mass measurement of neutral objects. The E864 strangelet search is conducted with the AGS Au beam impinging on various targets. The kinematics and acceptance of the apparatus limit the particle's energy range of interest to roughly 1–6A GeV. For instance, the mass 6 quark alpha predicted by Curtis Michael [34] would have, if produced in central Au + Pb collisions, an energy of the order of 12–18 GeV. Heavier objects [5] would have higher

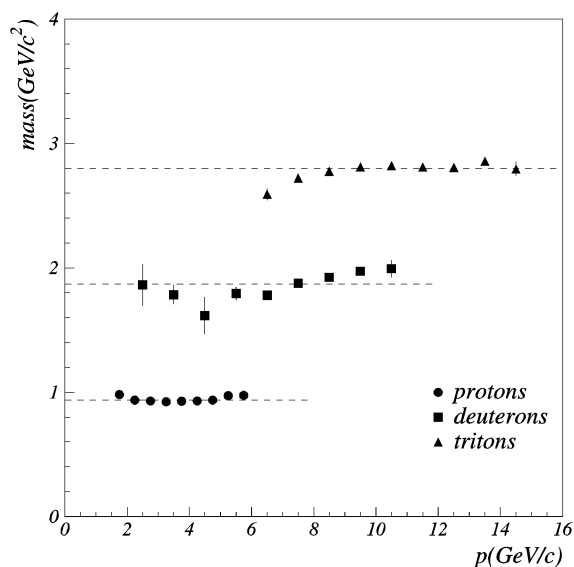


Fig. 28. Calorimeter reconstructed mass of protons (circles), deuterons (squares), and tritons (triangles) as a function of momentum. Dash lines show the p, d, and t masses.

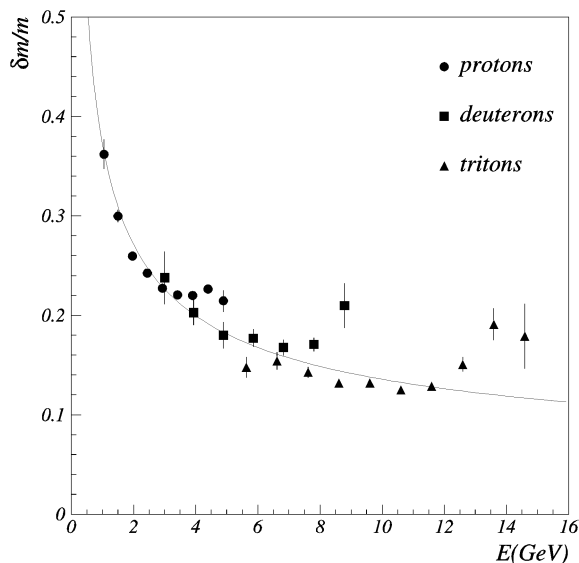


Fig. 29. Calorimeter mass resolution as function of particles energy for protons (circle), deuterons (square), and tritons (triangle). The mass reconstruction is based on the expression  $m = E/(\gamma - 1)$  where  $E$  is the deposited energy and  $\gamma = 1/\sqrt{1 - \beta^2}$ . The velocity  $\beta$  is computed from the TOF measured with the calorimeter. The solid line shows the function  $\delta m/m = 0.026 + 0.347/\sqrt{E(\text{GeV})}$ . Significant deviations from this curve are seen only for particles with  $\beta > 0.975$ .

energies accordingly. The mass resolution expected for mass 6 and heavier objects should thus be of the order of 10–15%. Lighter objects (neutron, anti-neutron, H-dibaryon [5]) are produced with lesser energies and should correspondingly be detected with a larger resolution of 25–30%.

### 5.8. Photo-electron yield

An important aspect of the calorimeter performance possibly affecting the energy resolution is the photon or photo-electron (p.e.) yield. Given the good resolution performance obtained by other experiments with a similar spaghetti design, it was estimated that the E864 design would yield a large number of photons per GeV and that the calorimeter response and energy resolution should not be dominated by the photon statistics. It is interesting to verify this prediction explicitly with experimental data. To do so, two different approaches were considered and found to yield similar values. The first method employed was to directly measure the number of photo-electrons produced by cosmic rays crossing the calorimeter towers transversely with a single photo-electron resolution phototube such as a Quanticon PMT. The second method relied on the laser input to each tower and used the assumption that the laser signal width as measured by all PMTs is determined mainly by photon statistics. The first measurement was made with a prototype tower section built with an early shipment of BCF-10 scintillating fibers. The statistical analysis is based on the full calorimeter implementation built with BCF-12 fibers.

A calorimeter tower section connected through a light guide to a Quanticon PMT was used to evaluate the number of photons produced in a tower by the passage of cosmic rays. The Quanticon PMT enabled a clear separation of the single photo-electron peak from the pedestal with a 13:1 signal-to-noise ratio. The ratio of the mean amplitude of the cosmic ray peak to the mean amplitude of the single photo-electron peak yields the mean number of photo-electrons produced by the transverse passage of cosmic rays in the fibers,  $20.86 \pm 0.18$ . This number is compared to the average energy deposited by cosmic rays,  $2.39 \pm 0.02$  MeV, as determined by GEANT. Addi-

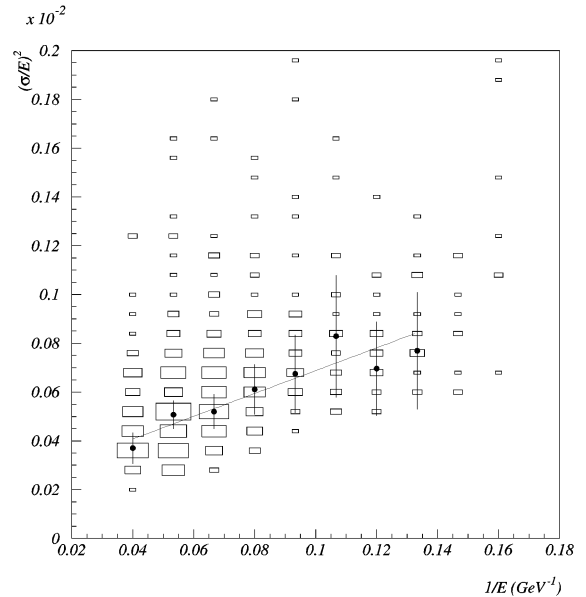


Fig. 30. Square of the relative laser signal width,  $\sigma/E$ , measured in all towers as a function of the inverse of the laser amplitude,  $E$ , expressed in GeV energy equivalent.

tionally, a 6 GeV proton was estimated, with GEANT, to deposit  $93.55 \pm 3.74$  MeV in the fibers. The photo-electron yield per GeV is thus estimated to be  $136 \pm 5$  p.e./GeV.

The laser light input into all towers was adjusted to produce large signals equivalent to that of 5–10 GeV particles. The light distribution system was designed to eliminate laser input fluctuations due to external causes, such as fluctuation of the laser spatial emission pattern. In particular, pulse-to-pulse amplitude variations of the laser output were corrected with the use of unity gain bi-planar PMTs. As described in Section 2.4, the corrected laser amplitude has a very narrow distribution and is likely to be dominated by statistical fluctuations of the photo-electron production. As the laser signals fed into each of the 754 towers have different amplitudes because of different injection and couplings, one can estimate the number of photo-electrons by considering the width of the laser signals as a function of their amplitude. If the amplitude fluctuations are dominated by photon statistics, the observed width should be proportional to the square root of the amplitude (proportional to the

number of photons). Fig. 30 shows a plot of the square of the relative laser signal width,  $(\sigma/E)^2$  determined in all towers as a function of the inverse of the measured laser amplitude,  $1/E$ , expressed in GeV energy equivalent. Although the entries in this plot are somewhat scattered due to additional sources of noise, one discerns a linear ridge forming at the bottom. The solid circles show the peaks of that ridge determined at regular intervals along the  $1/E$  axis. A fit to the data, shown as a solid line in Fig. 30, yields

$$(\sigma/E)^2 = (0.0022 \pm 0.0001) + (0.0047 \pm 0.0015)/E. \quad (9)$$

The fit has a  $\chi^2/\text{DoF}$  of 0.2. The finite constant term reflects the presence of additional sources of noise not related to the photon statistics. The  $1/E$  corresponds to the average energy deposition (GeV) per photo-electron. The photo-electron yield is thus estimated to  $217 \pm 68$  p.e./GeV.

The photon yields estimated with the two methods outlined above differ appreciably. The difference arises in part from the fact that BCF-10 fibers have a shorter attenuation length, a lower light yield, and have an emission peaked at a shorter wavelength. Improvements in the tower construction technique should also lead to a lesser attenuation and a better light collection. Thus, it is reasonable to expect a better photon yield per GeV with the tower built with BCF-12 fibers. In any case, the average photon yield is sufficiently large that statistical fluctuations of the yield should only have a modest impact on the energy resolution in the energy range of interest,  $> 2$  GeV, to the E864 experiment.

## 6. Summary and conclusion

The design and construction technique of a new hadronic lead scintillating fiber spaghetti calorimeter for AGS experiment E864 have been presented. The detector construction was completed prior to the 1995 AGS heavy ion run. The calorimeter was used, in conjunction with the rest of the E864 apparatus, to take data with a 11.6A GeV/c Au beam for a search of strangelets and the study of heavy ion collision dynamics.

Previously unpublished results obtained with a small prototype pertaining to the study of the energy response and the lateral shower profile have been presented. The energy response is observed to be non-Gaussian with a high side tail most prominent at the lowest energies examined. The high side tail is measured, to be exponential over 3 orders of magnitude, with a slope of  $-1.63 \pm 0.11/\text{GeV}$  in excellent agreement with a GEANT/FLUKA prediction of  $-1.51/\text{GeV}$ . It should not have any detrimental impact on the E864 search for strangelets and in fact should allow a significant improvement of the search sensitivity.

The lateral hadronic shower profile has been measured with the  $4 \times 3$  prototype. The profile measured is in qualitative agreement with measurements performed by the SPACAL [31] collaboration at higher energies with a calorimeter of similar design. The measured data are also reasonably well reproduced by a GEANT/FLUKA calculation although the FLUKA predictions tends to slightly overestimate the size of the long-range shower exponential tail.

Data from the 1995 heavy ion run have been analyzed to characterize the calorimeter performance. The calibration systems and methods have been described and their respective performance analyzed. The energy response to various particle species has been studied and no obvious saturation of the energy deposition was found for increasing particle mass. The calorimeter energy response was in fact observed to be linear within  $\pm 2\%$  for protons and  $\pm 5\%$  for light nuclei such as deuterons and tritons in the momentum range 1–4A GeV/c. The energy resolution was measured to be  $\delta E/E = (3.5 \pm 0.5)\% + (34.4 \pm 0.8)\%/\sqrt{E(\text{GeV})}$  in good agreement with a calculation performed with the Geant/Fluka package. Additionally, the TOF resolution was evaluated to be better than 400 ps over the 1–14 GeV energy range studied. The time-of-flight resolution measured in this work confirms results obtained with the prototype and published earlier [12]. The energy resolution measured with the full implementation significantly surpasses preliminary results presented in Ref. [12]. The improvement of the energy response and resolution results in part from ameliorations in the construction technique, in

particular the fiber end machining for light guide coupling, and in part from reduced noise and better PMT gain stability. The calorimeter mass resolution is dominated by the energy resolution and scales as  $1/\sqrt{E}$ . The observed mass resolution for protons, deuterons, and tritons are of the order of 28%, 18% and 14%, respectively, for particle's momenta ranging from 2 to 7A GeV/c. Similar or better mass resolutions are expected for heavier objects produced in the same rapidity range.

Overall, the calorimeter performance satisfies or exceeds the specifications and requirements set forth for the AGS E864 experiment.

### Acknowledgements

We gratefully acknowledge the excellent support of the AGS staff. This work was supported by grants from the Department of Energy (DoE) High Energy Physics Division, DoE Nuclear Physics Division, and the National Science Foundation.

### References

- [1] C. Pruneau et al. (E864 Collaboration), 2th Winter Workshop on Nuclear Dynamics, Snowbird, Utah, 3–10 February 1996; Proc. 6th Internat. Conf. on Calorimetry in High Energy Physics, 1996, Frascati, Italy, p. 261.
- [2] F. Rotondo et al. (E864 Collaboration), Proc. Quark Matter'96, 12th Internat. Conf. on Ultra-Relativistic Nucleus–Nucleus Collisions, Heidelberg, Germany, 20 May 1996.
- [3] J. Barrette et al., Phys. Lett. B 252 (1990) 550.
- [4] D. Beavis et al., Phys. Rev. Lett. 75 (1995) 3078.
- [5] E.P. Gilson, R.L. Jaffe, Phys. Rev. Lett. 71 (1993) 332.
- [6] T.A. Armstrong et al., in preparation.
- [7] J.G. Lajoie, Ph.D. Thesis Dissertation, Yale University, 1996.
- [8] D. Acosta et al., Nucl. Instr. and Meth. A 294 (1990) 193.
- [9] R. Brun et al., GEANT 3.12 User's Guide, CERN Data Handling Division, DD/EE/84-1.
- [10] P.A. Aarnio et al., FLUKA User's guide, Technical Report TIS-RP-190, CERN, 1987, 1990.
- [11] C.A. Pruneau et al., in preparation.
- [12] S.J. Bennett et al., Proc. 5th Internat. Conf. on Calorimetry in High Energy Physics, BNL, H.A. Gordon, D. Rueger (Eds.), World Scientific, Singapore, 1994, p. 361.
- [13] J. Hill et al., to be published.
- [14] J. Sandweiss et al., E864 Collaboration, Proposal for funding – Measurements of rare composite objects and high sensitivity searches for novel forms of matter produced in high energy heavy ion collisions (1991).
- [15] R. Wigmans, Nucl. Instr. and Meth. A 256 (1988) 273.
- [16] E. Bernardi et al., Nucl. Instr. and Meth. A 262 (1987) 229.
- [17] Bicron Corporation, Newbury, OH 44065-9677.
- [18] Philips Photonics, 100 Providence Pike, Slatersville, RI 02876.
- [19] Nanometric Systems Inc., 451 South Boulevard, Oak Park, IL 60302.
- [20] LeCroy Corporation, Chesnut Ridge, NY 10977-6499.
- [21] EG&G Ortec, 100 Midland Oak Ridge, TN 37831-0895.
- [22] CyberResearch Inc, Branford, CT 06405.
- [23] Laser Photonics Inc., 12351 Research Parkway, Orlando, FL 32826.
- [24] Labsphere Corporation, North Sutton, NH 03260.
- [25] Hamamatsu Corporation, Bridge Water, NJ 08807-0910.
- [26] Spectran Specialty Optics Company, 150 Fisher Dr., P.O. Box 1260, Avon, CT 06001.
- [27] DisplayTech Inc., 2200 Central Ave, Boulder, CO 80301.
- [28] H.C. Fesefeldt, Simulation of hadronic showers, physics and applications, Technical Report PITHA 85-02, III Physikalishes Institut, RWTH Aachen Physikzentrum, 5100 Aachen, Germany, September 1985.
- [29] R. Bellwied et al., Proc. 3rd Internat. Conf. on Calorimetry in High Energy Physics, Corpus Christi, TX, P. Hale, J. Siegrist (Eds.), World Scientific, Singapore, 1992, p. 604.
- [30] J.B. Birks, The Theory and Practice of Scintillation Counting, Macmillan, New York, 1964.
- [31] D. Acosta et al., Nucl. Instr. and Meth. A 316 (1992) 184.
- [32] R. Cernej, M.Sc. Thesis Dissertation, Wayne State University, 1996.
- [33] M. Fatyga et al., Nucl. Instr. and Meth. A 284 (1989) 323.
- [34] F. Curtis Michel, Phys. Rev. Lett. 60 (1988) 677.